https://doi.org/10.5194/wes-2026-69
Preprint. Discussion started: 23 April 2026

eawe european academy of wind energy
Open Access WIND ENERGY SCIENCE DISCUSSIONS

Controlling rigid-wing airborne wind energy systems during circular flight without exact path following

Duc H. Nguyen[1], Agustí Porta Ko[2,3], Tallak Tveide[3], Mark H. Lowenberg[1], and Espen Oland[3]

[1]School of Civil, Aerospace, and Design Engineering, University of Bristol, Bristol, BS8 1TR, United Kingdom
[2]Technical University of Denmark, Frederiksborgvej 399, 4000 Roskilde, Denmark
[3]Kitemill AS, Voss, 5704, Norway

Correspondence to: Duc H. Nguyen (duc.nguyen@bristol.ac.uk)

Abstract. We propose a simple feedback architecture that enables effective flight control of rigid-wing airborne wind energy systems during circular-pattern reel out. The controller performs well with only proportional-integral regulators, thereby presenting a significantly simpler solution compared to the existing literature. The key idea is in tracking the roll angle on a non-static reference frame, effectively reducing the control problem to one degree of freedom. This method of navigation does not require users to define an exact path for the kite to follow, which contributes to stability and robustness. In its minimum viable form, the controller can function with only ailerons while requiring no pitot-tube measurement, although the addition of elevators and rudder enables angle-of-attack and zero-sideslip tracking for more efficient power generation. Simulation-based verification is conducted on an industrial, 6-degree-of-freedom model with a flexible tether, nonlinear aerodynamics, and realistic wind conditions, showing satisfactory performance in all cases. Three expansions to the control law are then presented. The first one reduces angle of attack fluctuation during reel-out by adding a proportional pitch angle feedback term to the elevator, resulting in more power. In the second expansion, the reel-out radius is automatically adjusted to enable phase synchronisation of multiple kites in a farm configuration, where minimum separation rules may apply. The third expansion implements a simple proportional feedback rule that enables figure-of-eight flight. By using simple proportional-integral architecture, the controller is easy to implement, making it a suitable baseline system for benchmarking more advanced control laws.

1 Introduction

Airborne wind energy systems (AWES) are an emerging technology for electricity generation using tethered flying devices. Compared to traditional wind turbines, AWES are easy to transport and use less material over their lifetime. This means they can provide clean energy in areas where the construction of wind turbines is not feasible. Since its first formal conceptualisation by Loyd, 1980, AWES development has grown significantly in the past two decades, with research groups and startups proposing increasingly innovative designs. For an overview of the technology and its progression over the past decade, readers can refer to three systematic reviews published between 2015 and 2025 (Cherubini et al., 2015; Pereira and

https://doi.org/10.5194/wes-2026-69
Preprint. Discussion started: 23 April 2026

Sousa, 2023; Khurshid et al., 2025). Also worth mentioning are two books by Ahrens et al., 2013; Schmehl, 2018 that summarise key technical concepts.

Because AWES lack a solid structural foundation seen in conventional wind turbines, the number of degrees of freedom expands from 1 to 6. This fact places great emphasis on flight control for making AWES safe and efficient (Vermillion et al., 2021). Compared to free-flying aircraft, AWES differ by the fact that their natural motions during circular flights are limit cycles (self-sustained oscillations with fixed amplitude and frequency). Equilibrium solutions exist only when gravity is ignored and the circular trajectory is perpendicular to the wind (Trevisi et al., 2021; Trevisi, 2024; Nguyen et al., 2026a), although this trajectory is unachievable as half of the orbit has negative height (Nguyen et al., 2026a). Consequently, any realistic trajectory requires a feedback strategy that can handle self-oscillating dynamics, and the resulting control surface movements should also be cyclic. Closed-loop control in the presence of limit cycles is uncommon for fixed-wing airframes, although it is not unheard of. The X-15's flight control system uses adaptive gains that automatically increase until a small-amplitude limit cycle is achieved, which helps the aircraft achieve the highest gain possible without causing instability (Nasa, 1971).

An overview of many AWES controllers by Vermillion et al., 2021 shows that their algorithms are sophisticated. In the context of this paper, we can classify reel-out controllers into two categories: optimisation-based path planning and direct path planning. The former involves utilising an optimisation search (Cobb et al., 2020; Heydarnia et al., 2025) or reinforcement learning agent (Orzan et al., 2023; Basile et al., 2025) to find the best flight path that generates the most energy. The found path is a useful reference for quantifying the maximum power generation capability. However, deploying a pure optimisation-based controller on a real system introduces implementation complexity, especially due to many complex physical phenomena that are difficult or costly to model. Direct path planning involves designing a flight controller for a tethered aerial vehicle (rigid-wing aircraft or kites) to follow a predefined path in 3D space. Past works have covered waypoint-based guidance using L0- and L1-based control (Fernandes et al., 2022), defining the circular flight path as combinations of motion primitives (fundamental circles) (Vinha et al., 2025), and linking the reference path's geometry to the steering control law (Fagiano et al., 2014; Dief et al., 2020; Delosríos-Navarrete et al., 2025). These algorithms show great promise, and some have been verified experimentally (Fagiano et al., 2014; Dief et al., 2020; Delosríos-Navarrete et al., 2025). However, they require specialist knowledge to implement. Waypoint- and geometry-based guidance also split the control task into discrete steps, thereby creating a discontinuous controller that can complicate classical analysis. Cascaded nonlinear dynamic inversion control can provide continuous guidance with good tracking performance (Rapp et al., 2019), although successful deployment relies on accurate system modelling.

Therefore, it is desirable to have a simple control law with continuous guidance throughout the power production cycle. This paper proposes a solution for rigid-wing AWES – those that resemble fixed-wing aircraft with conventional control surfaces.

https://doi.org/10.5194/wes-2026-69
Preprint. Discussion started: 23 April 2026

eawe european academy of wind energy
Open Access WIND ENERGY SCIENCE DISCUSSIONS

An indirect path planning method is presented, which provides guidance during circular reel-out to ensure the flight path has the correct orientation and dimension, but does not specify the exact path for the kite to follow. Instead, circular flight emerges naturally as an inherent property of the controller. The resulting control surface movements are periodic, which are required for tethered circular flight as shown in our earlier trim analysis (Nguyen et al., 2026a). Simulation shows effective tracking, even when the reference path takes the kite away from the wind window. Therefore, the proposed guidance method can accommodate operational scenarios such as air/ground obstacle avoidance, height change for noise abatement (Schmidt et al., 2022), and reacting to a sudden change in wind direction. Deployment with a fixed-tether length is also possible, which enables the same control law to be used for ship-towing applications (Fritz, 2013). In the latter parts of the paper, we presented two extensions that reduces angle-of-attack oscillations and enable multi-kite synchronisation – both of which address key challenges in AWES operations.

The feedback architecture follows a cascaded control structure. Each loop closure fulfils a specific control objective as will be discussed in subsequent sections. Control gains are tuned empirically but obey the time scale separation principle, i.e., the gains in the outer layers should be an order of magnitude smaller than the inner layer gains. Higher performance can be obtained by employing classical methods for rigorous tuning, although the present system with empirically derived gains can already achieve all control objectives. Since the control algorithm is flight-path agnostic, both circular and figure of eight trajectories are possible.

2 Simulation environment

This study uses a 6-degree-of-freedom simulator of Kitemill's KM1 prototype – a 20 kW groundgen system driven by a fixed-wing unmanned aerial vehicle with mass 54 kg and wingspan 7.4 m (see Fig. 1). The aerial vehicle is referred to as a kite in this paper based on conventions adopted by the AWES community, which highlights the fact that the air vehicle extracts energy from the wind to remain airborne. Traditional trailing-edge control surfaces (aileron, elevator, and rudder) are used for flight control, in addition to flaps for increased lift during power production. The simulation was constructed in MATLAB & Simulink and, more recently, extended into Julia. Past studies that used the Simulink version can be found in references Mohammed et al., 2024b, Mohammed et al., 2024a; Rapp et al., 2019. In this paper, results with constant wind were generated in MATLAB & Simulink, while non-uniform wind analyses (section 4.2) were conducted in Julia but plotted in MATLAB for style consistency. Aerodynamic data of the KM1 airframe was obtained from computational fluid dynamics, which are dependent on angle of attack, sideslip angle, and control surface deflections. The total force and moment coefficients are calculated in a manner similar to Eqs. (3) and (5) in Rapp et al., 2019, which includes aerodynamic damping terms as functions of angular rates and airspeed. For illustrative purposes, a few key static aerodynamic relationships are shown in Fig. 2 to indicate the nonlinear dependencies of the force and moment coefficients with respect to the angles of incidence and sideslip.

https://doi.org/10.5194/wes-2026-69
Preprint. Discussion started: 23 April 2026

Figure 1. Aerial component of Kitemill's KM1 system.

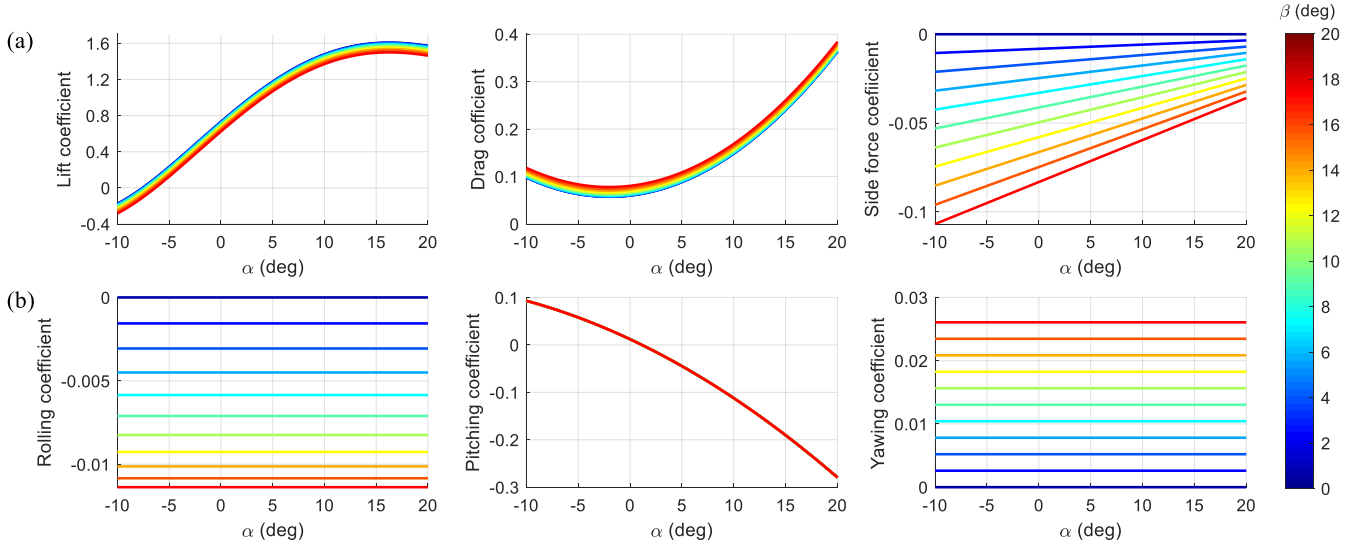

Figure 2. Static aerodynamic force (b) and moment (b) coefficients at full flaps and no control surface deflection.

In its open loop configuration, the simulator has 104 states, comprising 12 states to describe the aircraft's motion in 3D space, 2 states to describe the ground winch, and $6N$ states to model the flexible tether, where N is the number of tether nodes between the winch and the kite. The N nodes discretised the tether into $N+1$ segments, which are connected by second-order mass-spring-damper elements. If the tether's natural length is fixed, the winch states can be discarded, and the model reduces to 102 states. A detailed description of the equations of motion can be found in Rapp et al., 2019. Table 1 summarises the open-loop states, control surface inputs, and outputs.

https://doi.org/10.5194/wes-2026-69
Preprint. Discussion started: 23 April 2026

Table 1. Key elements of the open-loop simulation.

Aircraft states	Body-axis velocities: u, v, w Body-axis angular rates: p, q, r Earth-axis Euler angles: ϕ, θ, ψ Earth-axis coordinates: X, Y, Z
Winch states	Tether natural length: L Winch linear speed: $\dot{L}$
Tether states	Each node N has 6 states: its 3D Earth-axis coordinates and velocities. All results use N = 15 nodes.
Control surfaces	Ailerons: δ_a Elevator: δ_e Rudder: δ_r
Outputs	Angle of attack: α Sideslip angle: β Airspeed at the kite: V Instantaneous mechanical power: P Energy generated: E

The tether's natural length L (excluding elastic extension) is regulated by an ideal ground winch, which is modelled as a cylinder of mass m_w = 25 kg and has a constant radius of R_w = 0.25 m. The winch control system applies a winch force F_w that opposes the tether tension T at the winch. This gives a winch linear acceleration of

$$\ddot{L} = (T - F_w)\frac{R_w^2}{I_w} \tag{1}$$

where $I_w = 0.5 m_w R_w^2$ is the winch moment of inertia. The winch speed (reel-out speed) $\dot{L}$ and natural length L are found by integrating eq. (1) once and twice, respectively. Feedback control of the winch is provided by the term F_w, which is the output of a high-gain PID controller that tracks either a desired winch speed (keeping $\dot{L}$ close to constant) or a desired tether tension (keeping T close to constant). Apart from Fig. 24, all results in this paper with the winch active use the constant winch speed mode.

Provided that the winch is reeling out with positive tether tension, the instantaneous mechanical power P is calculated as

$$P = T\dot{L} \tag{2}$$

https://doi.org/10.5194/wes-2026-69
Preprint. Discussion started: 23 April 2026

eawe european academy of wind energy
Open Access WIND ENERGY SCIENCE DISCUSSIONS

and assuming no losses in the winch, Eq. (12) can be integrated to give the total energy generated up to time t

$$E = \int_{t_{L=350}}^{t} P\, dt \tag{3}$$

where $t_{L=350}$ is the simulation time at the start of reel out, defined to be when the tether's natural length is 350 m. Reel out ends when L reaches 700 m.

3 Baseline controller design

3.1 Key concept: tilting the reference plane

The principal idea of the proposed flight control system involves tracking the Euler roll angle on a reference plane that is not the ground. This reference plane and the flat Earth coordinate systems are shown in Fig. 3. The kite's Cartesian coordinates and Euler angles with respect to the ground are labelled $[X, Y, Z]$ and $[\phi, \theta, \psi]$, respectively (see Fig. 3a). The $[X, Y, Z]$ set aligns with the north, east, and down directions, and the Euler angles $[\phi, \theta, \psi]$ denote roll, pitch, and yaw. $[X, Y, Z]$ = [0, 0, 0] corresponds to the location of the ground winch. This point is also defined to be the origin of the reference plane, as shown in Fig. 3b. Two angles λ_R (lambda for eLevation) and ζ_R (zeta for aZimuth) describes the reference plane's orientation with respect to the ground, such that when $\lambda_R = \zeta_R = 0^o$, the reference plane's three principal axes X_R, Y_R, and Z_R align with the Earth's up, west, and south directions. The kite's Euler angles on the reference plane are denoted $[\phi_R, \theta_R, \psi_R]$. These angles facilitate easy understanding of the kite's orientation with respect to the wind. For instance, assuming that the wind travels from south to north and $\lambda_R = \zeta_R = 0^o$ as shown in Fig. 5a, the ideal flight trajectory with the wing perpendicular to the wind will have $\phi_R = \theta_R = 0^o$, i.e., zero pitch and roll angle with respect to the reference plane. The wind direction in Fig. 5 is used for the rest of the paper with a speed of 14 m/s, unless otherwise noted. Subsequent analysis does not require the use of the kite's yaw angle ψ_R on the reference plane. To simplify illustrations, a single dashed line originating from the winch and pointing in the reference plane's up direction is used to indicate the reference plane's orientation (see Fig. 3b).

The reference plane's role in flight control is now discussed. Consider the feedback scheme in Fig. 4 with three proportional-integral (PI) loops. For convenience, following shorthand notation for PI control is used throughout the paper

$$PI(x_{SP}, x) = K_P(x_{SP} - x) + K_I \int (x_{SP} - x)\, dt \tag{4}$$

where x_{SP} and x are the set point (SP) and feedback signal, while K_P and K_I are the proportional and integral gains.

https://doi.org/10.5194/wes-2026-69
Preprint. Discussion started: 23 April 2026

eawe european academy of wind energy
Open Access WIND ENERGY SCIENCE DISCUSSIONS

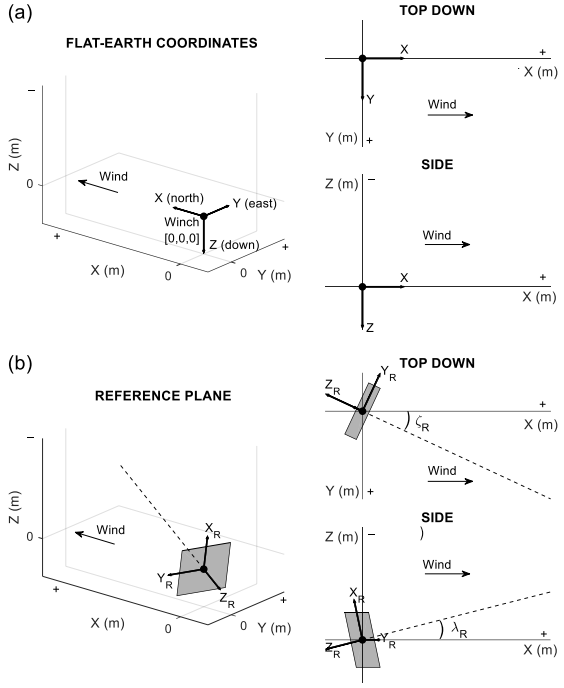

Figure 3. Two coordinate systems: Earth (a) and reference plane (b).

155

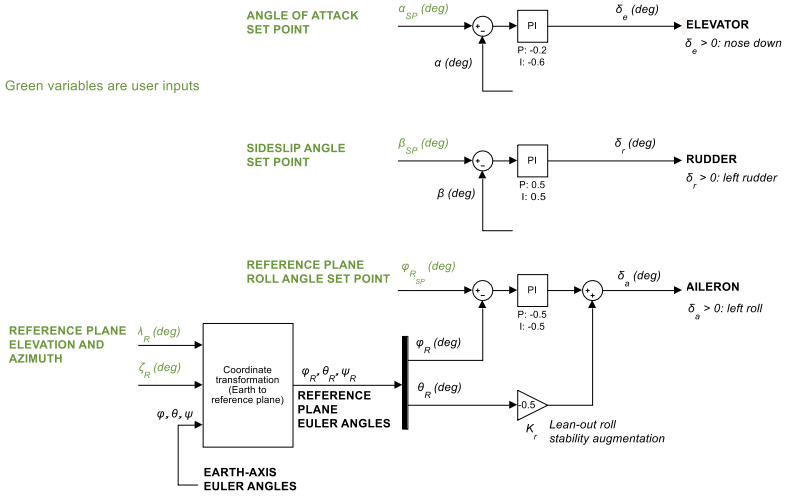

Figure 4. Basic flight control system (subsequently referred to as the inner loop). The Earth-to-reference-plane coordinate transformation is presented in appendix A.

160 Pitch and yaw control are achieved by tracking the desired angle of attack α and sideslip angle β using the elevator and rudder, respectively. For the ailerons, their role is to track a demanded roll angle $\phi_{R_{SP}}$ on the reference plane. This feedback

https://doi.org/10.5194/wes-2026-69
Preprint. Discussion started: 23 April 2026

eawe european academy of wind energy
Open Access WIND ENERGY SCIENCE DISCUSSIONS

arrangement implies that the reference plane's orientation $[\lambda_R, \zeta_R]$ is known. These two angles are treated as static user inputs in this section. Accordingly, the three control surfaces are governed by the following feedback law

$$\delta_e = PI(\alpha_{SP}, \alpha) \tag{5}$$

$$\delta_r = PI(\beta_{SP}, \beta) \tag{6}$$

$$\delta_a = PI\left(\phi_{R_{SP}}, \phi_R\right) + K_r \theta_R \tag{7}$$

The second term in Eq. (7) multiplies the reference-plane pitch angle by a proportional gain K_r. This pitch cross feeding into ailerons counteracts the roll instability encountered in large-radius tethered circular flight, which was first reported in one of our earlier studies (see the discussion surrounding Eq. (1) in (Nguyen et al., 2026a)). The sign of K_r reflects flight direction. For trajectories where the circle's centre is on the port (left) wing's side, K_r should be negative.

To illustrate the feedback scheme presented in Fig. 4, we now examine a closed-loop response with the tether length fixed (i.e., $\dot{L} = \ddot{L} = 0$) at 350 m – a typical length at the start of reel out. The reference plane orientation is $[\lambda_R, \zeta_R]$ = [0°, 0°], and a representative combination of set points $[\alpha_{SP}, \beta_{SP}, \phi_{RP_{SP}}]$ = [6°, 0°, –15°] is chosen. Negative $\phi_{RP_{SP}}$ indicates the circle centre is on the port side of the wing, which is assumed throughout this paper without loss of generality. In this arrangement, the kite follows a circular orbit as shown in Fig. 5a. Inspecting the time history of this trajectory (Fig. 5b) reveals that the controller has entered a small limit cycle with periodic forcing inputs. This behaviour is expected, as our previous work in Nguyen et al., 2026a has shown that tracking a set of specified α, β, and ϕ_{RP} using fixed control surfaces (i.e., an equilibrium response) is only possible when gravity is ignored. The resulting gravity-free orbit is normal to the wind and has its circle centre overlapping the winch when viewed from the wind-facing direction. When gravity is included as shown in Fig. 5a, we see the circle centre shifting downward due to weight and a slight sideways due to lift asymmetry (from the wind-facing view: the kite climbs at the 3 o'clock position and descends at the 9 o'clock point, so the latter generates more lift, pushing the orbit centre to the side). Gravity also changes direction periodically with respect to the kite's body axis throughout the cycle. All of the above factors mean that the desired closed-loop trajectory is a limit cycle, so control surface movements should be cyclic to counteract the external periodic disturbance. Nevertheless, all three controlled variables α, β, and ϕ_{RP} oscillate with small amplitudes around the desired values, and the cyclic control surface movements are also small.

https://doi.org/10.5194/wes-2026-69
Preprint. Discussion started: 23 April 2026

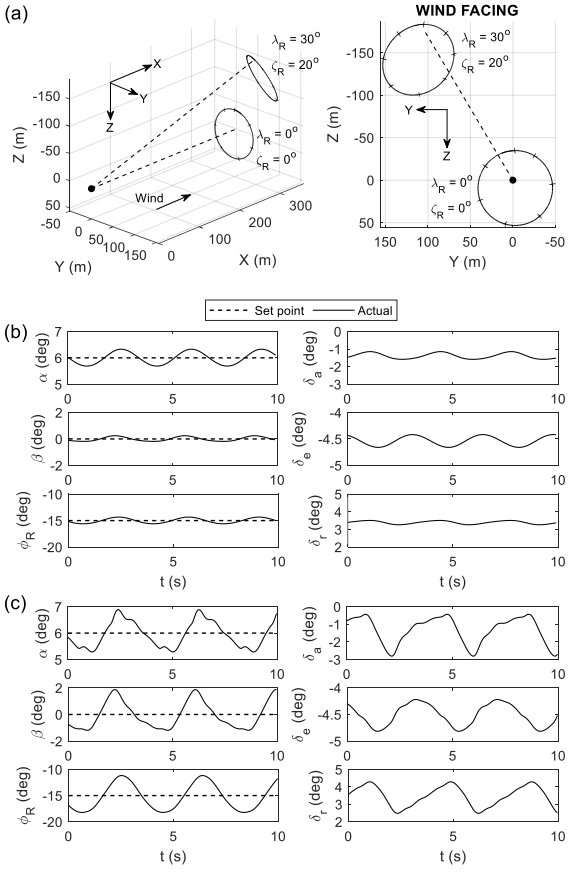

Figure 5. Closed-loop trajectories (a) and time histories (b and c) with two different reference plane orientations. The time histories of $[\lambda_R, \zeta_R]$ = [0°, 0°] and $[\lambda_R, \zeta_R]$ = [30°, 20°] are shown in (b) and (c), respectively.

The reference plane orientation is now changed to non-trivial values of $[\lambda_R, \zeta_R]$ = [30°, 20°]. Figure 5a shows the resulting closed-loop response. The kite still follows a circular path, which is now at a slight angle to the wind due to the new reference plane's orientation. Larger magnitudes in λ_R and ζ_R result in more longitudinal and lateral shifting, which become less effective as the circular orbit moves further away from its ideal location of being normal to the wind (achieved only when gravity is ignored and $[\lambda_R, \zeta_R]$ = [0°, 0°]). A consequence of shifting further away from the ideal location is higher limit cycle amplitudes, as seen in Fig. 5c vs Fig. 5b. This behaviour is congruent with our previous observations, which noted that circular flight further away from the ideal location requires larger cyclic control inputs (Nguyen et al., 2026a). Nevertheless, as long as there is enough control power and sufficient wind to prevent airspeed from dropping to the stall point, the current flight control scheme will keep the kite in a stable circular orbit.

https://doi.org/10.5194/wes-2026-69
Preprint. Discussion started: 23 April 2026

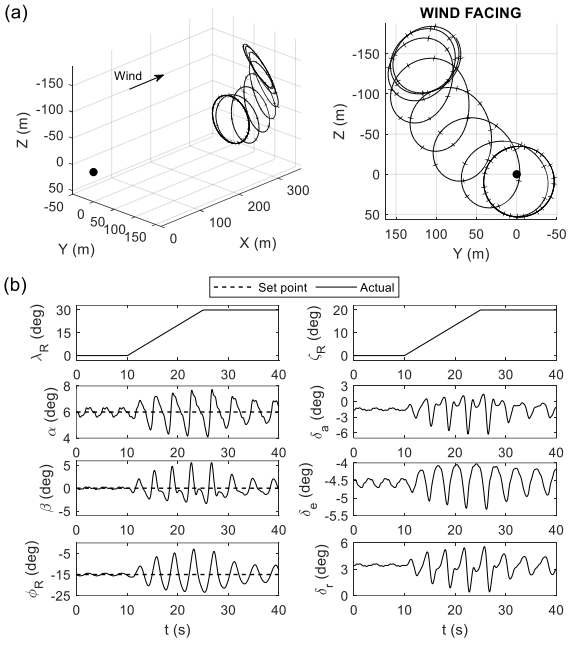

Figure 6. Response to simultaneous ramp inputs in λ_R and ζ_R.

Results in Fig. 5 suggests that the orbit centre can be dynamically shifted by adjusting the reference plane's orientation. To demonstrate this point, Fig. 6 shows the kite's response to two simultaneous ramp inputs in λ_R and ζ_R. Both ramps last 15 seconds, starting from $[\lambda_R, \zeta_R] = [0^o, 0^o]$ and ending at $[\lambda_R, \zeta_R] = [30^o, 20^o]$. The resulting trajectory shows that the kite achieves a gradual transition between the two conditions while maintaining circular flight throughout the manoeuvre. This method of transitioning between different operating points is more desirable than taking a straight-line path to the destination, which risks running out of airspeed mid-flight due to the lack of a dedicated propulsion unit. The fact that the kite maintains circular flight by itself also simplifies control design significantly, as there is no need to design the exact path in 3D space for the kite to follow. In other words, the path-planning problem is reduced to adjusting two variables λ_R and ζ_R by the right rate and magnitude.

Lastly, to adjust the circle radius, one simply needs to change the set point for the reference plane roll angle $\phi_{R_{SP}}$. Our previous work has shown that leaning more into the turn reduces the radius, while leaning out widens the orbit (Nguyen et al., 2026a). In this example of a left-turning trajectory, increasing the radius requires a more positive ϕ_R. Figure 7 shows two circular trajectories corresponding to $\phi_{R_{SP}} = -15^o$ and 0^o. It can be seen that the 0^o case achieves a larger radius as intended.

This section has shown that by using the ailerons to track a fixed roll angle on a user-defined reference plane, the kite can keep itself in circular orbit without requiring complex path planning. Tilting the reference plane (i.e., adjusting λ_R and ζ_R)

https://doi.org/10.5194/wes-2026-69
Preprint. Discussion started: 23 April 2026

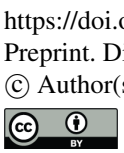

eawe european academy of wind energy
Open Access WIND ENERGY SCIENCE DISCUSSIONS

provides a means to shift the circular orbit to a desired location. Additionally, the radius can be widened or tightened by changing the set point for the reference plane roll angle. These ideas provide the foundation for a circular reel-out controller, which is described in the following section.

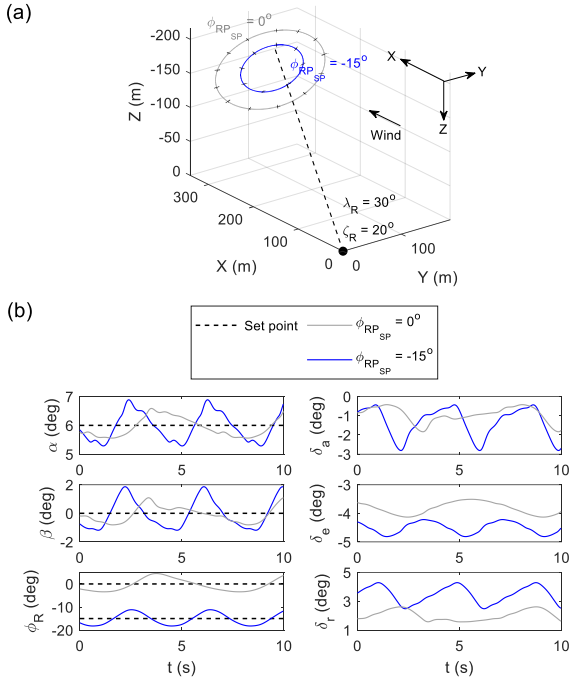

Figure 7. Closed-loop trajectories (a) and time histories (b) with different $\phi_{R_{SP}}$ values.

3.2 Flight control during reel out

During circular reel out, the kite's trajectory resembles a helical sweep similar to a spring that wraps around a cylinder. This imaginary cylinder is shown in light blue in Fig. 8. The cylinder can be defined by the following parameters:

- Originates from the point P with Earth-axis coordinates P_X, P_Y, and P_Z.
- Has radius R_{SP}.
- Has orientation defined by the elevation and azimuth angles λ_R and ζ_R as shown in Fig. 8.

To track the kite's location with respect to the cylinder, we use the vector $[X_P, Y_P, Z_P]$ based on a third set of coordinates originating from the point P (shown in the top plot of Fig. 8). These three axes form a 'production plane'. Note that the definitions of production and reference planes are similar with only one difference: the production plane does not have to originate from the winch at $[X, Y, Z] = [0, 0, 0]$.

https://doi.org/10.5194/wes-2026-69
Preprint. Discussion started: 23 April 2026

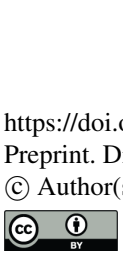

eawe european academy of wind energy
Open Access WIND ENERGY SCIENCE DISCUSSIONS

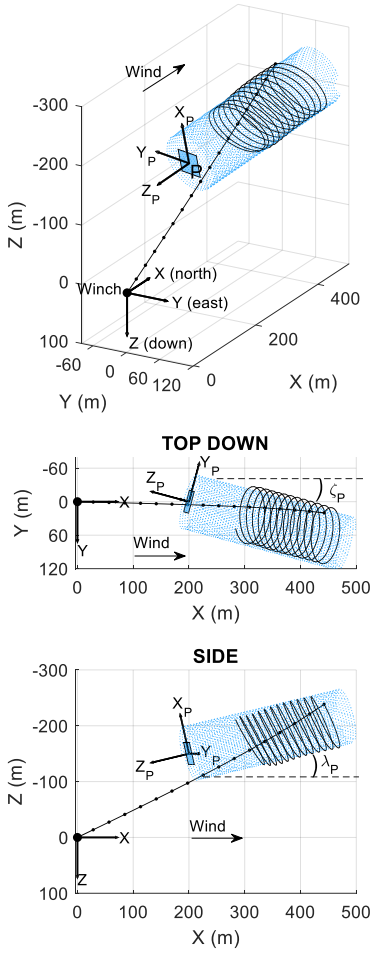

240

Figure 8. Reference cylinder (light blue) and the production plane (blue square).

An example reel-out trajectory (with the tether visible) is depicted in Fig. 8. This helical flight path that wraps around the cylinder has its production plane coordinates X_P and Y_P oscillate about zero, resulting in its actual radius $R = \sqrt{X_P^2 + Y_P^2}$ equals to the desired radius R_{SP}. The 'wrap around' definition does not specify an exact path for the kite to follow, which simplifies the controller significantly and contributes to its stability. To achieve this desired reel-out trajectory, three additional PI loops are added to the flight control system to automate the three user inputs shown in Fig. 4:

- λ_R is adjusted to keep the production-plane coordinate X_P at zero.
- ζ_R is adjusted to keep the production-plane coordinate Y_P at zero.
- $\phi_{R_{SP}}$ is adjusted to keep the production plane radius $R = \sqrt{X_P^2 + Y_P^2}$ equal to the desired radius R_{SP}.

https://doi.org/10.5194/wes-2026-69
Preprint. Discussion started: 23 April 2026

Figure 9 is full block diagram. The components previously presented in Fig. 4 form the inner loop, while three new PI elements form the outer loop. Note that a low-pass filter with time constant τ = 10 sec is used on the R feedback path to reduce $\phi_{RP_{SP}}$ oscillation since large changes in radius can be achieved by a gradual adjustment in $\phi_{RP_{SP}}$. The resulting outer loop is described by Eqs. (8-11):

$$\dot{R}_{filtered} = -\frac{1}{\tau}R_{filtered} + \frac{1}{\tau}R \tag{8}$$

$$\phi_{R_{SP}} = PI(R_{SP}, R_{filtered}) \tag{9}$$

$$\lambda_R = PI(0, X_P) \tag{10}$$

$$\zeta_R = PI(0, Y_P) \tag{11}$$

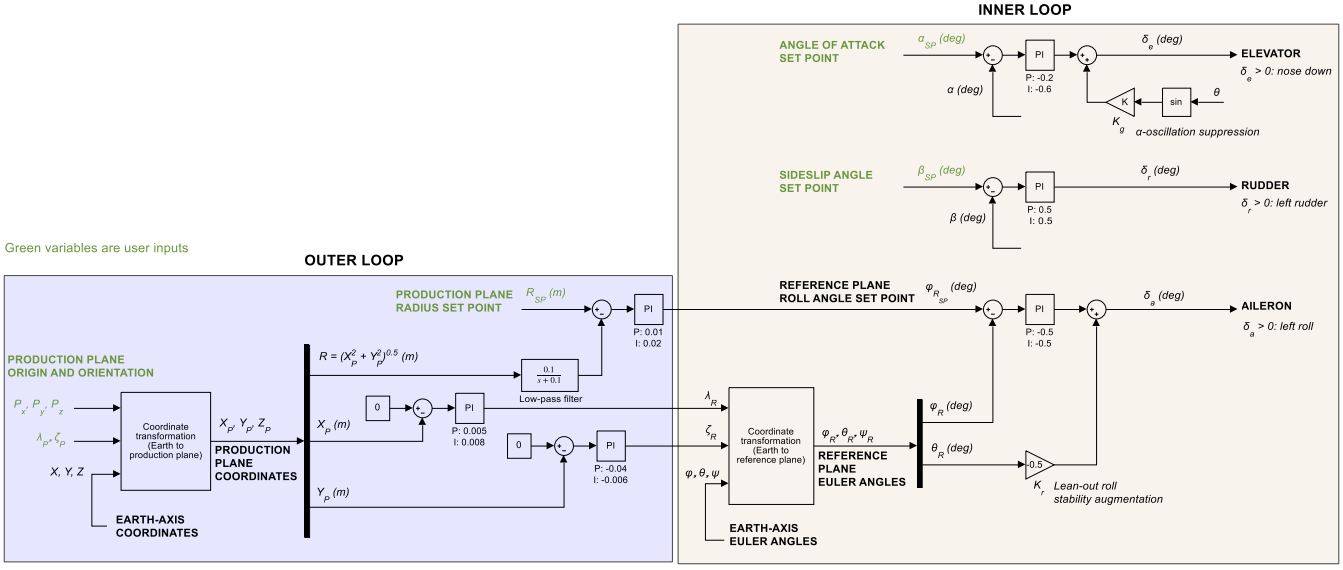

Figure 9. Full flight control system. The Earth-to-production-plane coordinate transformation is presented in appendix B.

Using this feedback law, the guidance task has been reduced to a one-degree-of-freedom problem handled by one set of control surface (the ailerons). Note that the inner loop in Fig. 9 shows an optional $K_g \sin\theta$ feedback path to the elevator. This term reduces the angle of attack oscillation amplitude and is only used in Section 6.

https://doi.org/10.5194/wes-2026-69
Preprint. Discussion started: 23 April 2026

eawe european academy of wind energy
Open Access WIND ENERGY SCIENCE DISCUSSIONS

4 Simulation results

4.1 Uniform wind

A typical reel-out trajectory is presented in Fig. 10, which has 75 m radius and a slight 13° climb angle (via λ_P) to reduce the risk of the tether scraping the ground. The kite successfully archives reference tracking in angle of attack, sideslip, and cylinder wrap-around. Note the second column in Fig. 10b, which shows the three output variables λ_R, ζ_R, and $\phi_{R_{SP}}$ of the outer loop that are used as input to the inner loop. All three parameters require gradual adjustment as the tether length extends to compensate for increasing tether drag. By conventional feedback control standard, the variation in radius can be considered large, reaching 15% above the set point toward the end of reel out. Nevertheless, the 3D trajectory suggests that this variation still results in a reasonable trajectory. Control surface usage increases as the tether length increases due to higher tether mass and drag, resulting in lower airspeed and hence reduced control effectiveness. Therefore, a limiting factor in how far the kite can reel out is control travel saturation (in addition to other efficiency issues that can be studied with an optimisation algorithm).

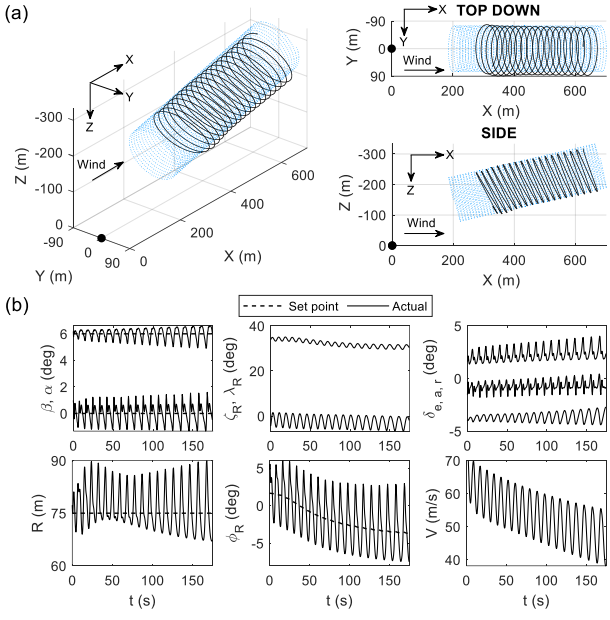

Figure 10. A typical circular reel-out trajectory with parameters P = [200, 0, -150] m, [λ_P, ζ_P] = [13°, 0°], and R_{SP} = 75 m. The winch speed is kept constant at 2.0 m/s.

To further stress-test the controller, tracking performance with less ideal reel-out paths is now examined. Figure 11 shows a diagonal reel out, which is achieved by setting ζ_P to 15°. Sideway reel out is shown in Fig. 12, where both ζ_P and λ_R are 0°, but the reference cylinder is shifted to the side by 100 m. Both instances show the kite successfully tracking the blue cylinder despite higher lateral force from the tether. Therefore, the controller is deemed to have satisfactory performance in uniform wind.

https://doi.org/10.5194/wes-2026-69
Preprint. Discussion started: 23 April 2026

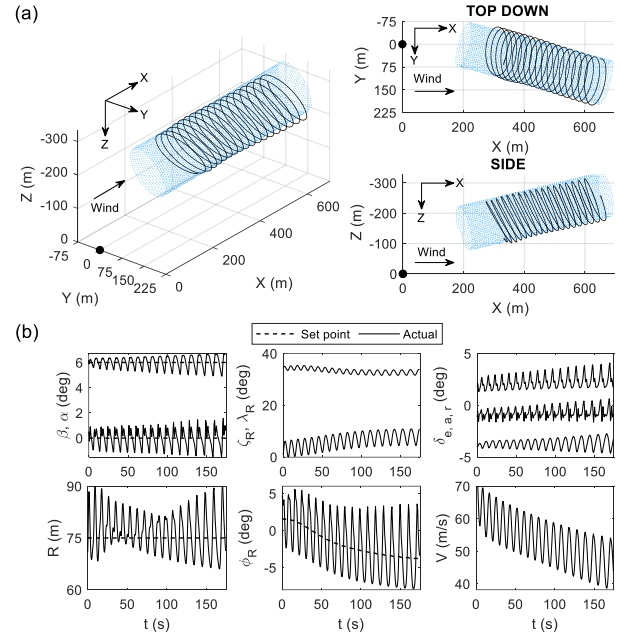

Figure 11. Diagonal reel out with parameters P = [200, 0, -150] m, [λ_P, ζ_P] = [13°, 15°], and R_{SP} = 75 m. The winch speed is kept constant at 2.0 m/s.

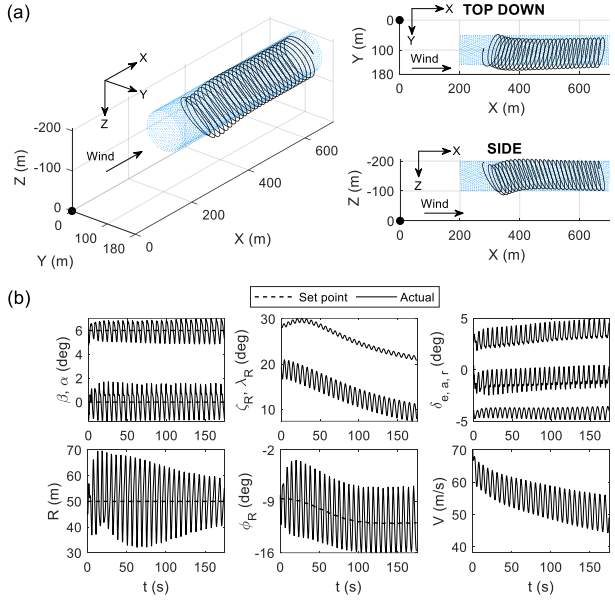

Figure 12. Sideway reel out with parameters P = [200, 100, -150] m, [λ_P, ζ_P] = [0°, 0°], and R_{SP} = 50 m. The winch speed is kept constant at 2.0 m/s.

4.2 Non-uniform wind with turbulence

Experiments have shown that there is considerable variation in wind speed with height, so a feasible controller must be able to perform in a non-uniform wind field. The simulation is now augmented with realistic wind and turbulence conditions. Two wind fields shown in Fig. 13 are used. The first one (referred to as medium wind) has an average speed of 12.1 m/s at 150 m height, and the second one (high wind) averages at 22.9 m/s at 100 m. Both wind fields were derived from LIDAR data at Kitemill's test site in Lista, Norway, on two different days. Variations in the wind profile over time are also captured in the Lidar data as shown in Fig. 13 and implemented in the simulation.

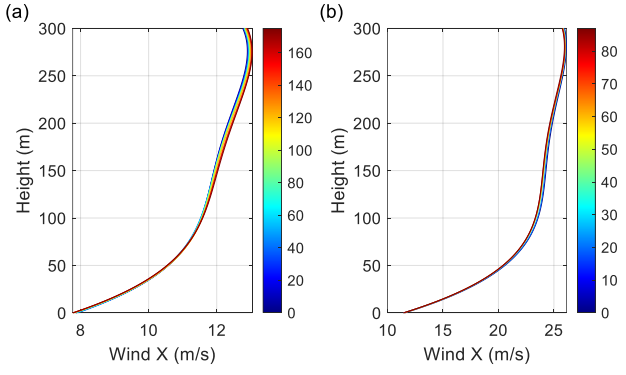

Figure 13. Medium (a) and high (b) wind fields implemented in the simulation based on LIDAR data.

https://doi.org/10.5194/wes-2026-69
Preprint. Discussion started: 23 April 2026

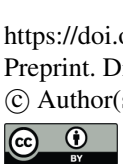

eawe european academy of wind energy
Open Access WIND ENERGY SCIENCE DISCUSSIONS

Additionally, LIDAR measurements at the site have shown that atmospheric turbulence is present, resulting in significant disturbances in both wind speed and direction. To capture this phenomenon, we implemented a turbulence box based on the Mann model (Mann, 1994). This box covers the 3D space flown by the kite with local wind velocity fluctuations due to atmospheric turbulence. Such fluctuations are added to the wind velocity seen by the kite as the turbulence box is convected downstream with the mean wind speed. Generating the turbulence box requires the Mann model parameters: dominant turbulence length scale L_M, amplitude parameter $\alpha\varepsilon^{2/3}$ and anisotropy parameter Γ. The turbulence length scale and amplitude parameter have been estimated from flow field parameters (Kelly, 2018) measured by the Lidar at the test site. Two different turbulence cases have been employed in the simulations according to the turbulence measured at the site, referred to as medium turbulence ($\alpha\varepsilon^{2/3}$=0.0108) and high turbulence ($\alpha\varepsilon^{2/3}$= 0.0267). The turbulence length scale has been defined as L_M =78.44m for both cases, being representative of the site, while the anisotropy parameter has been assumed as Γ = 3.0.

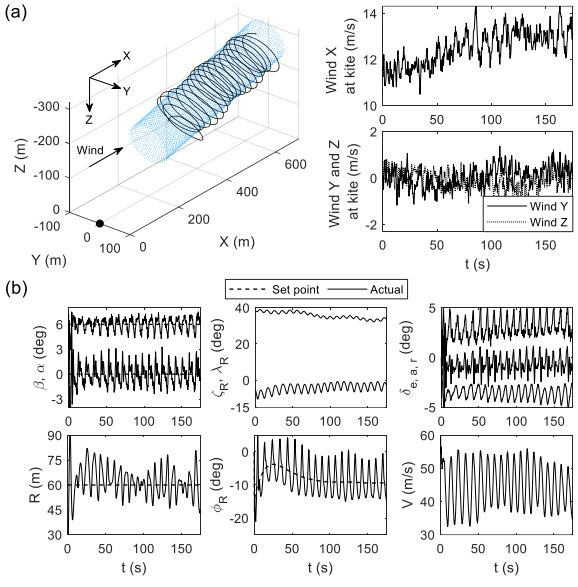

Figure 14. Reel out in medium wind and medium turbulence. The winch speed is kept constant at 2.0 m/s. A better tracking performance can be achieved by reducing the winch speed.

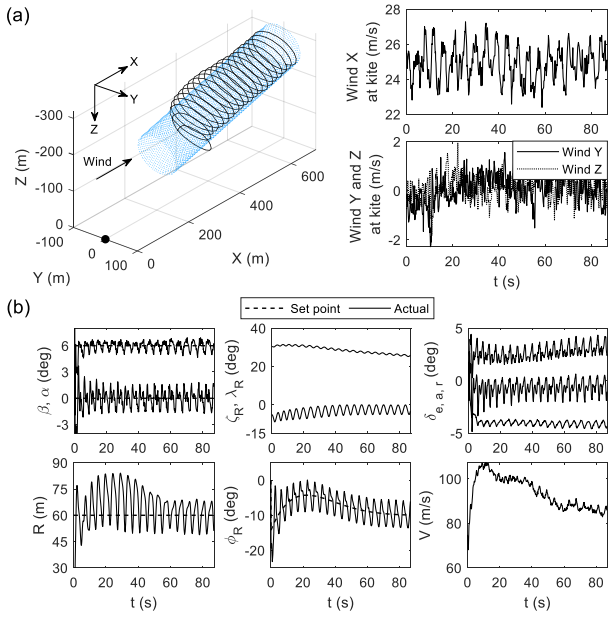

Figure 15. Reel out in high wind and high turbulence. The winch speed is kept constant at 4.0 m/s.

Figure 14 shows the closed-loop response to medium wind and medium turbulence, and Fig. 15 is for high wind and high turbulence. The first case (Fig. 14) exhibits notably poorer tracking. This is caused by the reduced control surface effectiveness at low airspeed during reel out, which becomes noticeable on the KM1 at airspeed below 35 m/s. The combination of wind gradient and turbulence creates multiple instances of the airspeed dropping below 35 m/s, leading to reduced tracking performance. A potential remedy for flying in such conditions is to reduce winch speed, which increases

https://doi.org/10.5194/wes-2026-69
Preprint. Discussion started: 23 April 2026

the apparent wind speed at the kite and results in higher airspeed. Conversely, the high wind and high turbulence case in Fig. 15 exhibits much better performance, despite significantly larger local wind speed fluctuation in all three directions. An even faster convergence to the blue cylinder can be achieved if the gains are tuned for high wind. Nevertheless, both simulations have demonstrated that the controller can provide accurate tracking in realistic wind conditions. Good performance can be expected when the airspeed is kept above 30 m/s, whether through flying in higher wind speed, reeling out slower, or both. A method to improve flight performance in low wind by dynamically varying the winch reel-out speed will be presented in a future publication.

This paragraph concludes the analysis with non-uniform wind. For the rest of the paper, a 14 m/s uniform wind field with no turbulence is assumed.

5 Discussions

5.1 Winch speed control

Since our flight control system does not specify an exact flight path, the 'wavelength' of the resulting helical trajectory is dependent on winch control, not flight control. Figure 16 shows two reel-out cycles with the same reference path and wind conditions but different winch speeds. Reeling out faster creates more sparsely spaced loops, which produces more energy (since mechanical power equals tether tension times winch speed) but reduces the apparent wind speed at the kite. If the apparent wind drops too much, the airframe can stall. A detailed study on the interaction between the winch and flight control for power generation can be found in Nguyen et al., 2026b. In the context of this paper, we have shown that the flight control system can track the reference cylinder at any winch speed that does not cause the airframe to stall.

5.2 Radius control with large error signal

Figure 17a shows the kite joining a sideway reel out from outside the reference cylinder. A bottleneck point is seen, which is caused by the radius controller. At the starting point, the radius error is large, so the radius tracker tightens the turn to compensate for the large error signal. This manoeuvre can excessively reduce the radii of the enroute circular loops, causing potential control problems. To avoid the bottleneck problem, radius control should be turned off until the kite is already inside the reference cylinder. Figure 17b shows the kite rejoining the same cylinder but with $\phi_{RP_{SP}}$ manually set to -3^{o} at the start, which resulted in no bottleneck. Once inside the cylinder, radius tracking can be safely turned on.

https://doi.org/10.5194/wes-2026-69
Preprint. Discussion started: 23 April 2026

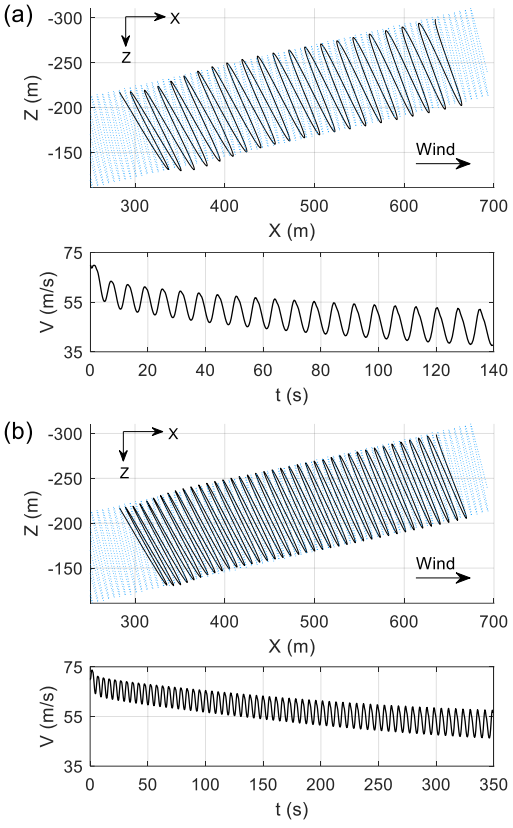

Figure 16. Reeling out at 2.5 m/s (a) and 1.0 m/s (b) winch speed, showing lower airspeed in (a) due to faster reel out.

360

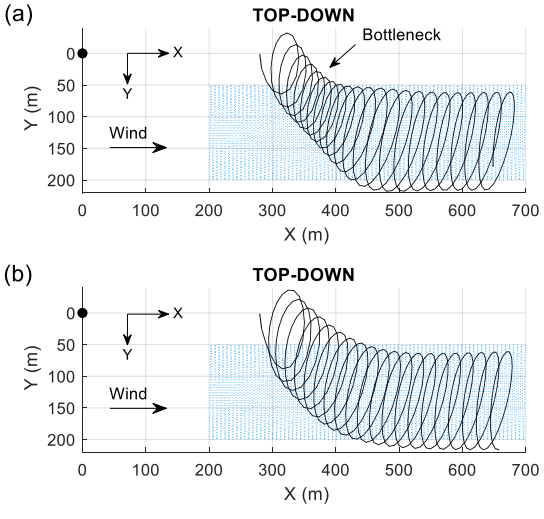

Figure 17. Bottleneck issue caused by enabling radius tracking when the kite is far outside the cylinder: (a) with radius tracking deployed, (b) without radius tracking.

https://doi.org/10.5194/wes-2026-69
Preprint. Discussion started: 23 April 2026

eawe european academy of wind energy
Open Access WIND ENERGY SCIENCE DISCUSSIONS

5.3 Cosine losses at high altitudes

Early AWES literature has note the cosine loss phenomenon, where given the same wind speed, power is reduced at higher altitudes (Diehl, 2013). This reduction is caused by a misalignment between the aerodynamic force and the wind vector. In the context of circular reel out, flying higher means individual orbits are angled further away from their ideal position of being 90° to the wind. The misalignment between aerodynamic force and wind direction increases, resulting in power reduction. A demonstration is provided in Fig. 18, which analyses three horizontal reel-out trajectories with same radii (50 m) but different target heights (reflected by different values for P_z, which is the Z coordinate of the reference cylinder origin):

- Solid line: ideal trajectory orbiting the centre of the wind window with P_z = 0 m and no gravity. This flight path is not achievable in test flights due to the negative heights.
- Dashed line: 100 m height with gravity. This trajectory can be considered realistic.
- Dotted line: 250 m height with gravity.

The kite with highest altitude experiences more control difficulty, but notably produces 46% less power than in the ideal case. As altitude increases, the angle between individual circular orbits and the wind drops below the ideal value of 90°, which is achieved only when P_z = 0 m with no gravity. Due to this increasing misalignment with height, the wind contributes less to pulling the tether out, resulting in less power generated. Whilst flying higher also increases tether drag and reduces power, the contribution from the cosine loss is more significant. If the kite at P_z = −250 m was to achieve 21.9 kW (same power output as with P_z = −100 m), the wind speed must increase to 17 m/s.

5.4 Minimum viable controller: ailerons only

Since all outer-loop signals are combined into just one control surface input (ailerons – see Fig. 9), the kite can follow the reference cylinder with elevator and rudder fixed. Figure 19 shows one such example, where rudder is kept neutral and elevator is set t o −4°. Power production is less efficient without active angle of attack and sideslip monitoring, but being able to test the flight controller without pitot tubes (for α and β measurements) can be useful for rapid development of new AWES prototypes. Mathematically speaking, flying with only one active control surface is possible because the goal of tracking a constant radius – regardless of the flight path taken – is a one degree-of-freedom problem. This formulation of feedback control reduces complexity and implies that a different control effector can be used. Indeed, test flights at Kitemill have successfully flown circular reel out using only rudder (ailerons and elevator are fixed), although simulations show that this method is less efficient for power generation than using ailerons (Nguyen et al., 2026b).

https://doi.org/10.5194/wes-2026-69
Preprint. Discussion started: 23 April 2026

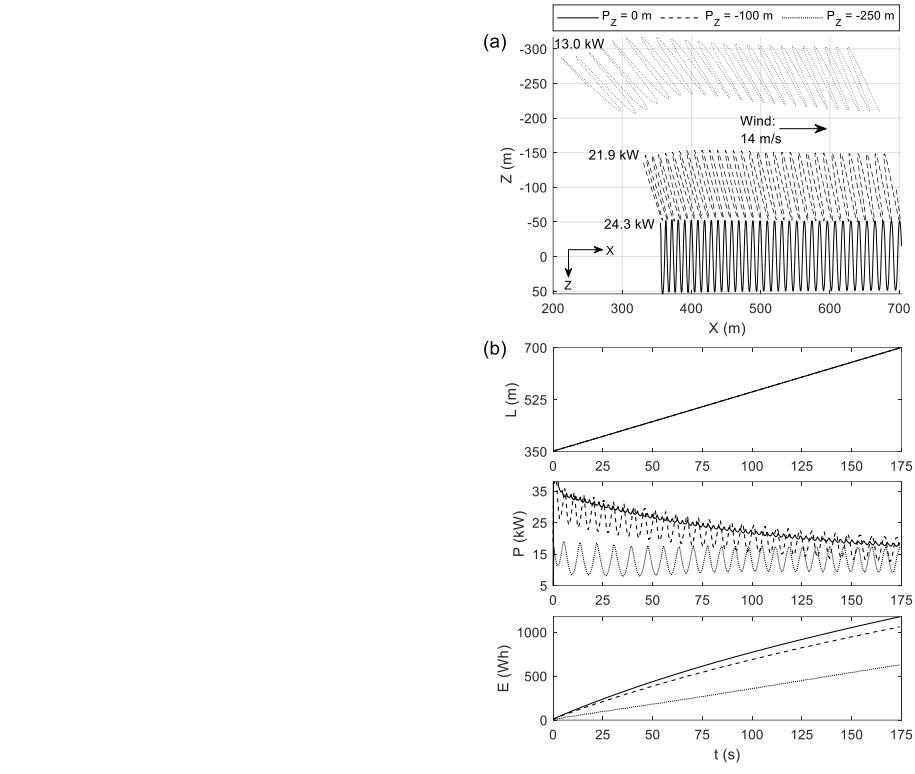

Figure 18. Different power production capacities at different heights due to cosine loss.

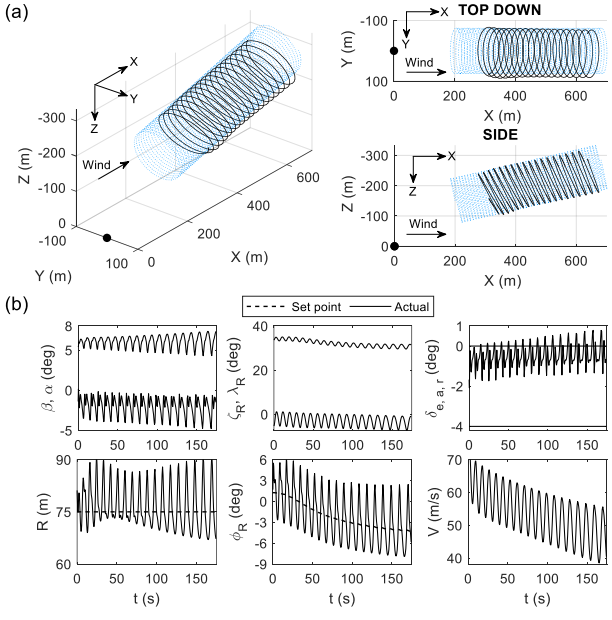

Figure 19. Normal reel out flown with fixed elevator (−4°) and rudder (0°). Parameters: P = [200, 0, -150] m, [λ_P, ζ_P] = [13°, 0°], and R_{SP} = 75 m. The winch speed is kept constant at 2.0 m/s.

https://doi.org/10.5194/wes-2026-69
Preprint. Discussion started: 23 April 2026

eawe european academy of wind energy
Open Access WIND ENERGY SCIENCE DISCUSSIONS

5.5 Semi-manual mode

The kite can be flown using only the inner loop – even with the winch active. We refer to this configuration as the 'semi-manual mode'. Figure 20 shows an example. Five set points have to be specified by the user as shown in Fig. 4, namely $\phi_{R_{SP}}$, λ_R, and ζ_R for the ailerons, α_{SP} for the elevator, and β_{SP} for the rudder (noting that the last two can also kept fixed as discussed in section 5.4). With λ_R sufficiently high for satisfactory ground clearance and ζ_R not too far off the wind direction, the kite can sustain safe circular reel out. Steering the reel-out path can be achieved by manually adjusting λ_R and ζ_R, while radius adjustment be done with $\phi_{R_{SP}}$.

For initial AWES control development, we recommend flying in semi-manual mode with the tether length fixed, gravity disabled, and λ_R and ζ_R set to 0°. Doing so enable the kite to converge to an equilibrium state by circling a point at zero height. From here, the α_{SP}, β_{SP}, and $\phi_{R_{SP}}$ loops can be tuned using classical methods.

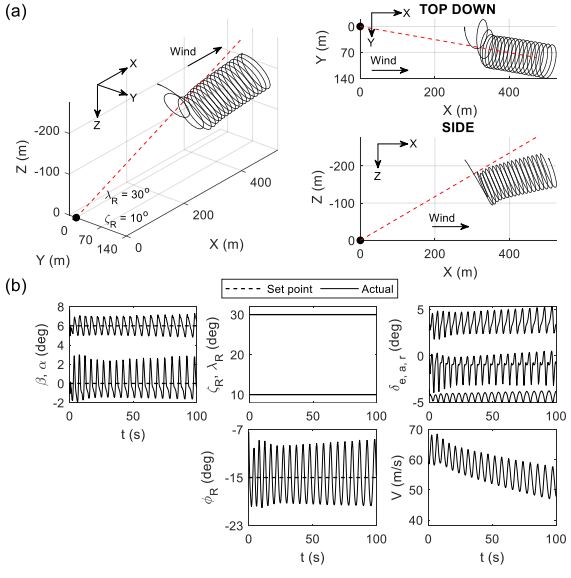

Figure 20. Semi-manual flight using only the inner loop.

5.6 Limit cycles

A potential downside of the controller is that it cannot converge to an equilibrium. To demonstrate, consider the full flight control system in a gravity-free environment with $[\lambda_P, \zeta_P] = [0°, 0°]$ and fixed tether length as shown in Fig. 21a. The resulting circular trajectory is perpendicular to the wind, and past work has shown that an equilibrium trim point exists in this condition (i.e., no cyclic control surface movement required) (Nguyen et al., 2026a). However, Fig. 21b shows that λ_R and ζ_R still exhibit small limit cycles caused by the integrated production-plane coordinates X_P and Y_P in the error signal. All three control surfaces are also in limit cycles as a result. These limit cycles disappear when λ_R and ζ_R are manually set to

https://doi.org/10.5194/wes-2026-69
Preprint. Discussion started: 23 April 2026

zero, at which point, the kite can be linearised for inner-loop control design. For the outer loop, the small-amplitude limit cycles can be ignored during manual tuning, but they may pose a challenge for rigorous control design. Further discussions on analysing nonlinear limit-cycle systems can be found in maths textbooks such as Jordan and Smith, 2007.

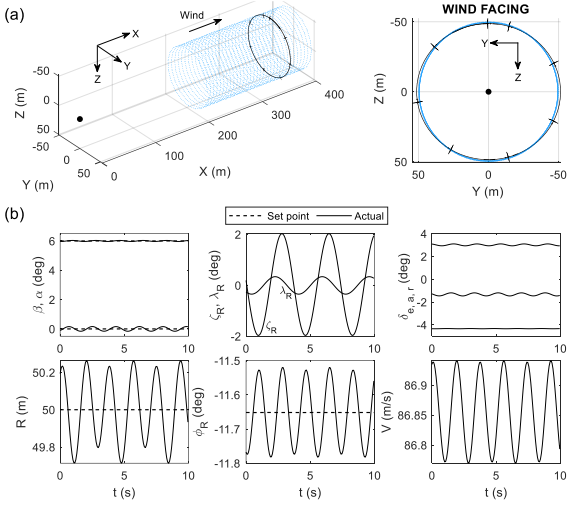

Figure 21. Closed-loop limit cycles, which is always present in the full flight controller even when equilibrium trim is possible.

6 Extension 1: reducing angle-of-attack oscillation

Although limit cycles cannot be eliminated, some can be reduced in amplitude. Angle of attack is one prime candidate for this reduction, since flying at a near-constant α keeps the airframe close to its optimal lift-to-drag state, which improves power generation. Two elements contribute to angle-of-attack oscillation during circular reel out: changing apparent wind direction at different points in the circle and changing gravity direction with respect to the airframe's body axis. Whilst the former is unavoidable, the latter can be reduced. Assuming no external wind, gravity's contribution can be seen in the last term of Eq. (12):

$$\dot{\alpha} = q - \frac{1}{2}\frac{\rho V S}{m} C_L - (p\cos\alpha + r\sin\alpha)\tan\beta + \frac{g}{V}\left(\frac{\cos\phi\cos\theta\cos\alpha + \sin\theta\sin\alpha}{\cos\beta}\right) \tag{12}$$

This is one of the standard 6-degree-of-freedom equations of motion for aircraft, but written in the aerodynamic wind axis (α, β, V) instead of the more common body axis velocities (u, v, w). If the contribution of gravity in Eq. (12) can be cancelled out using feedback control, angle-of-attack oscillation will be significantly reduced. This gravity term can be decomposed into two components

https://doi.org/10.5194/wes-2026-69
Preprint. Discussion started: 23 April 2026

$$\dot{\alpha}_{g_z} = \frac{g}{V}\frac{\cos\phi\cos\theta\cos\alpha}{\cos\beta} \tag{13}$$

$$\dot{\alpha}_{g_x} = \frac{g}{V}\frac{\sin\theta\sin\alpha}{\cos\beta} \tag{14}$$

where $\dot{\alpha}_{g_z}$ describes how the body-axis (not Earth-axis) vertical component of gravity affects angle of attack, and $\dot{\alpha}_{g_x}$ reflects the contribution of the longitudinal component. Comparing both variables against α in Fig. 22, one can see that $\dot{\alpha}_{g_x}$ is roughly in phase with α and oscillates about zero, whereas $\dot{\alpha}_{g_z}$ has a slight phase lead and is offset from zero. Both properties of $\dot{\alpha}_{g_x}$ suggest that it can be used as a feedback signal on the elevator channel to cancel out the angle-of-attack oscillation. This is possible in the simulation. However, $\dot{\alpha}_{g_x}$ in Eq. (14) has three quantities that require measurements from a pitot tube: V, α, and β. If all three are removed from Eq. (14), the right-hand side reduces to just $g\sin\theta$. Figure 22 shows that this term has similar phase and offset properties as the full $\dot{\alpha}_{g_x}$ equation. Therefore, the feedback signal to the elevator can be simply $K_g\sin\theta$, where K_g is a proportional gain equal to g multiplied by a constant. This additional feedback path creates the second junction in the elevator path (see Fig. 9). As such, the augmented pitch control law is

$$\delta_e = PI(\alpha_{SP}, \alpha) + K_g\sin\theta \tag{15}$$

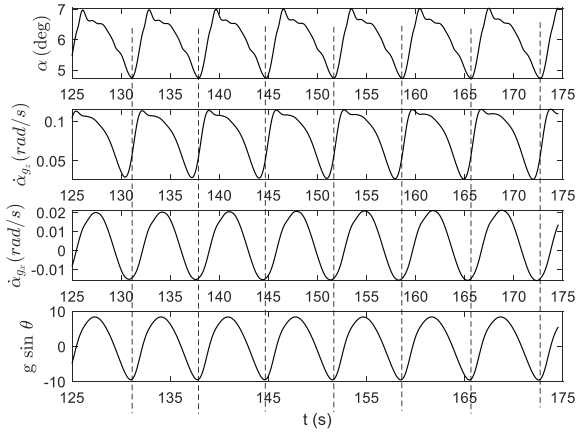

Figure 22. Potential feedback terms to cancel out the effect of gravity on α oscillation.

Figure 23 shows the effect of the new pitch control law on angle of attack and power generation over a normal reel-out trajectory but with a low radius of 50 m to exaggerate α oscillation. The dashed line labelled 'K_g = 0' indicates flying with without the α suppression controller. It can be seen that the controller successfully suppresses the limit cycle in α and provides a marginal 0.1 kW gain in power. This power gain is more noticeable if a less ideal winch is used. In Fig. 24, the

https://doi.org/10.5194/wes-2026-69
Preprint. Discussion started: 23 April 2026

same reel-out trajectory is flown again but with a winch that maintains a constant tether tension of 8 kN. This winch control mechanism is less efficient for power generation (Nguyen et al., 2026b), but is closer to what has been tested experimentally at Kitemill. In this arrangement, angle of attack oscillation has been significantly reduced. The kite experiences less aerodynamic drag as a result and completes the production cycle 14 seconds faster – a 0.9 kW gain in power. Inspecting the elevator movement in both Fig. 23 and Fig. 24, we can see that the new pitch control law has phase-shifted the cyclic elevator input and also demands more elevator travel compared to the $K_g = 0$ case, resulting in the desired α-suppression effect. This behaviour reflects the fact that our proposed control law is a form of dynamic inversion.

Since gravity's contribution is independent of the chosen flight path, the angle-of-attack suppression controller also works with figure-of-eight reel out. This capability is demonstrated in section 8. Appendix C presents the stability proof of the controller.

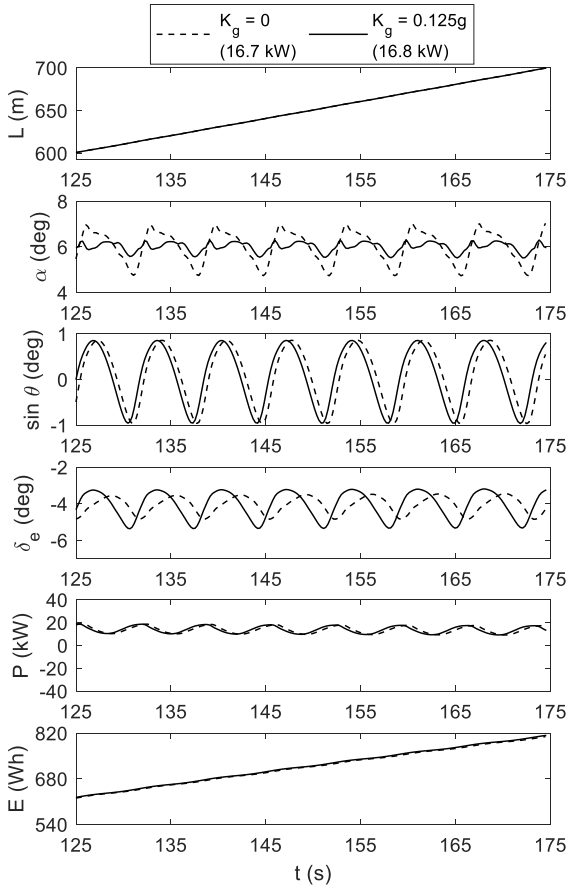

Figure 23 Effect of the α-suppression controller. The winch speed is constant at 2 m/s.

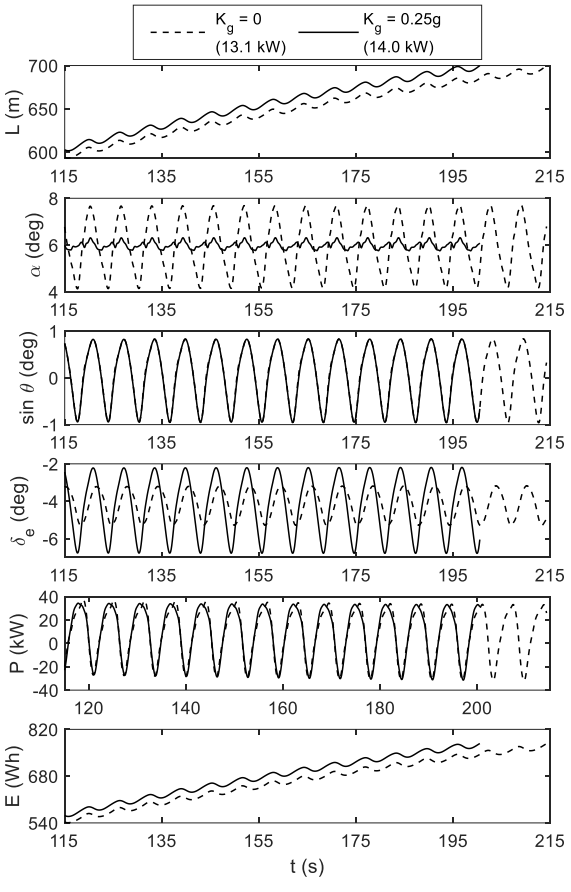

Figure 24 Effect of the α-suppression controller. The winch tracks a constant tether tension of 8 kN.

https://doi.org/10.5194/wes-2026-69
Preprint. Discussion started: 23 April 2026

eawe european academy of wind energy
Open Access WIND ENERGY SCIENCE DISCUSSIONS

7 Extension 2: multi-kite synchronisation

Our proposed flight controller can be extended to synchronise multiple kites in a farm configuration, where a minimum separation rule may be in place. The working principle is based on the fact that without a dedicated propulsion unit, the kite's angular velocity in the cylinder is dependent primarily on radius. Faster sweep is achieved by lowering the radius, and vice versa. Figure 7 provides an example. Within the same 10-second window, the blue trajectory with a smaller radius completes around 2.5 orbits, whereas the grey one does only 1.5. Therefore, phase synchronisation of multiple kites can be achieved by adjusting the radius. To demonstrate, consider a hypothetical two-kite farm scenario in Fig. 25. Two reference cylinders with 80 m radius are placed with only 100 m in lateral separation between their centre lines, leading to 60 m of overlap in the Y direction. Both kites have their winches placed at the origin – an unlikely scenario as the winches are likely to be separated laterally in real life. However, we chose the origin to create a sideway reel out situation, which is more challenging for the controller. The angular phase Ω of each kite in its reference cylinder is defined as

$$\Omega = \text{atan2}(Y_P, X_P) \tag{16}$$

Note that Ω = 0° corresponds to the kite being at the highest point of the circle.

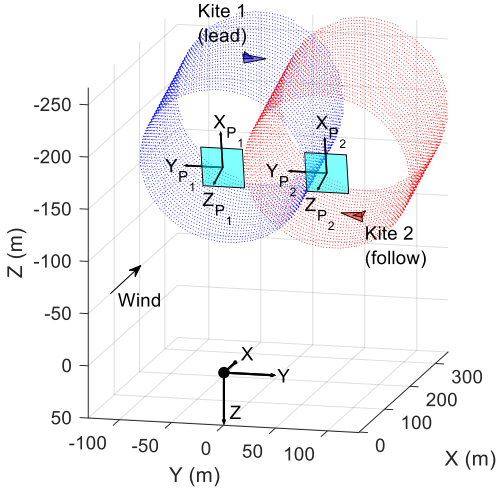

Figure 25. Starting location of the two kites for synchronisation testing.

The lead kite is flown normally using the control scheme in Fig. 9. For the second kite, the radius set point R_{SP_2} is automatically adjusted using an additional PI loop presented in Fig. 26. This controller seeks to match the second kite's phase with the first kite's by adjusting the second kite's radius. To prevent overcorrection, the output R_{SP_2} of the phase-synchronisation controller is limited to between 60 m and 100 m, which is no more than ±20 m from R_{SP_1} = 80 m.

https://doi.org/10.5194/wes-2026-69
Preprint. Discussion started: 23 April 2026

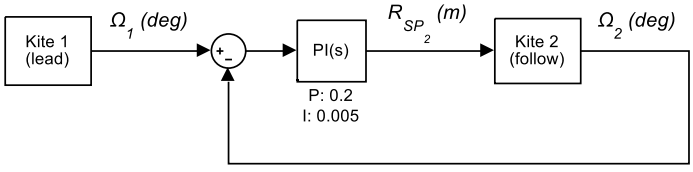

Figure 26. Phase synchronisation controller in the second kite.

The phase synchronisation controller is now tested with two kites starting from a 180-degree out-of-phase position as shown in Fig. 25. Longitudinal separation is provided by the different starting tether lengths: 350 m for kite 1 and 300 m for kite 2. The resulting trajectories in Fig. 27 show successful synchronisation after 40 seconds, or roughly 3 loops. Once the phase gap is closed, the second kite remains in sync for the rest of the reel-out cycle.

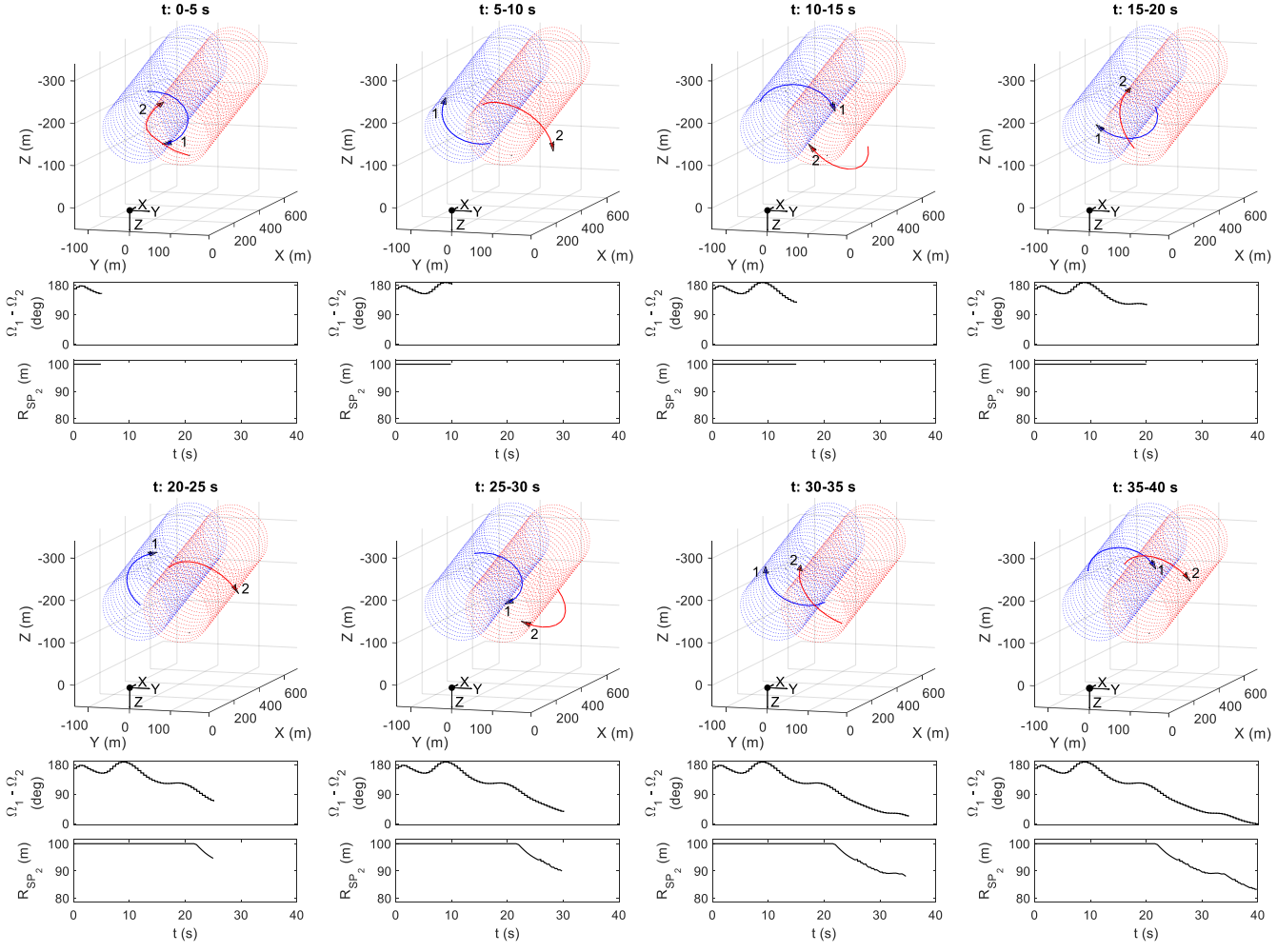

Figure 27. Simulation result of the phase synchronisation controller.

https://doi.org/10.5194/wes-2026-69
Preprint. Discussion started: 23 April 2026

eawe european academy of wind energy
Open Access WIND ENERGY SCIENCE DISCUSSIONS

8 Extension 3: figure-of-eight flight pattern

The proposed control framework can be adapted to fly figure-of-eight (henceforth abbreviated to 'F8') patterns using a proportional feedback law. Although this method does not provide full navigation capabilities as seen in circular-flight analysis, it is sufficient as a demonstrator for rapid simulator development and verification. Consider a generic F8 pattern as shown in Fig. 28a. The production plane location is now shifted to the winch at the origin with the elevation and azimuth angles λ_P and ζ_P set to zero. In this configuration, the axis Z_P points in the opposite direction of the wind. Using the same definition of angular phase Ω from Eq. (16), we have the evolution of Ω over two F8 cycles as shown in Fig. 28b. This evolution resembles the amount of roll on the production plane required to fly an F8 path. Near the centre of lemniscate (point A), this roll angle crosses zero, reaching its peak positive and negative values at C or B (depending on whether an eight-up or eight-down pattern is flown). The phase angle Ω can therefore be used as the feedback signal to change the reference plane roll angle set point using a proportional control law with gain K_8

$$\phi_{R_{SP}}\,[deg] = K_8 \Omega\,[deg] \tag{17}$$

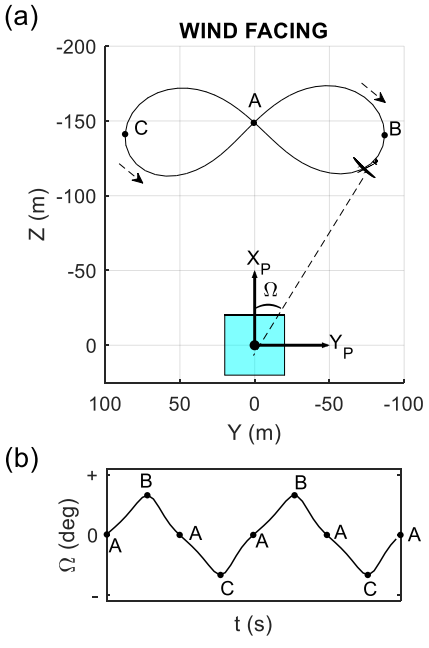

Figure 28. A generic figure-of-eight pattern (a) and evolution of the phase angle over two cycles.

where the sign of the proportional gain K_8 determines if the trajectory is eight-up or eight-down. Setting a larger magnitude for K_8 means a tighter turn when the kite reaches the edge of the lemniscate, resulting in a narrower F8 trajectory. The aileron control law requires a minor modification

https://doi.org/10.5194/wes-2026-69
Preprint. Discussion started: 23 April 2026

$$\delta_a = PI\left(\phi_{R_{SP}}, \phi_R\right) + K_r \theta_r K_s \phi_{RP_{SP}} \tag{18}$$

noting that the roll stiffness term is now multiplied by a factor $K_s\phi_{RP_{SP}}$, with K_s being another proportional gain. This addition accommodates the fact that the roll stiffness gain K_r must change sign depending on which side of the lemniscate the kite is flying on. Because $\phi_{RP_{SP}}$ has a smooth zero crossing near centre of the lemniscate, this signal can be used to indicate sign change after appropriate scaling by K_s to keep the peak magnitude of $K_s\phi_{RP_{SP}}$ close to 1. In all subsequent results, K_s is fixed at –0.05. Figure 29 shows the block diagram of the F8 controller. The only user input available (beyond control gains) is the reference plane elevation angle λ_R. All other guidance parameters must be set to zero to avoid instability caused by the limited steering capability of the proportional control law, which requires symmetry in the lemniscate to function properly.

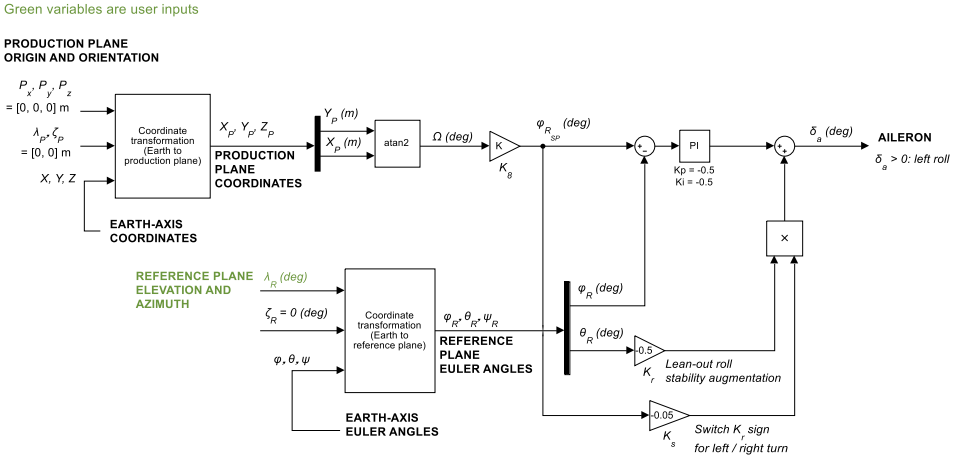

Figure 29. Block diagram of the figure-of-eight flight controller for aileron. Note that the elevator and rudder loops remain unchanged.

The controller's performance is now assessed. Figure 30 shows a few F8 patterns with positive and negative gains. As discussed, the lemiscate's width can be reduced by increasing K_8 magnitude. To fly at a higher elevation, λ_R should be increased as shown in Fig. 31.

https://doi.org/10.5194/wes-2026-69
Preprint. Discussion started: 23 April 2026

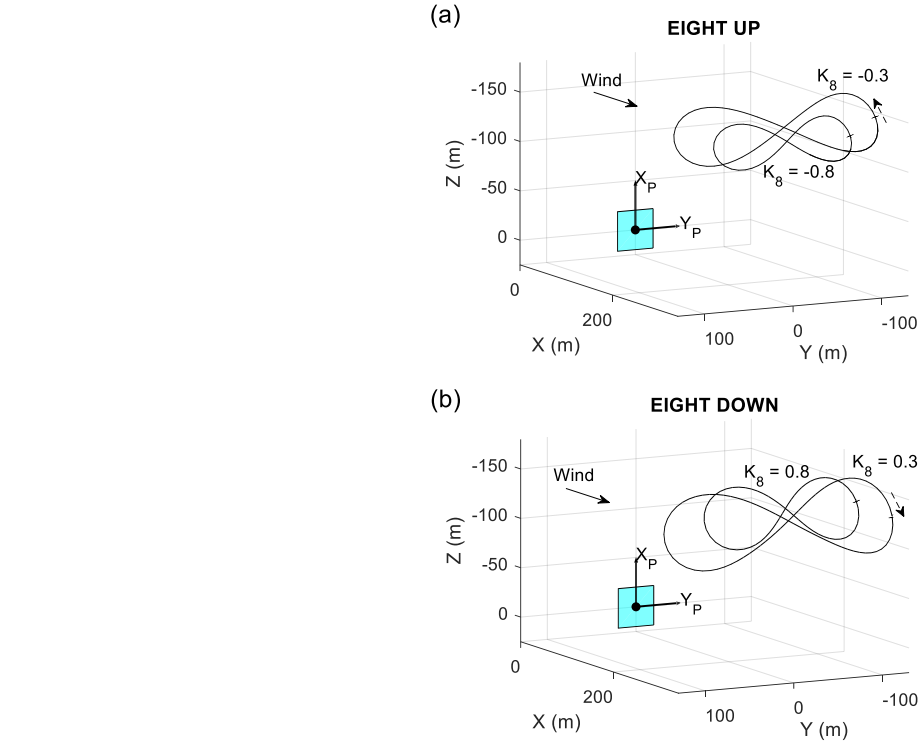

Figure 30. Eight-up (a) and eight-down (b) trajectories at $\lambda = 25^o$ with different control gains.

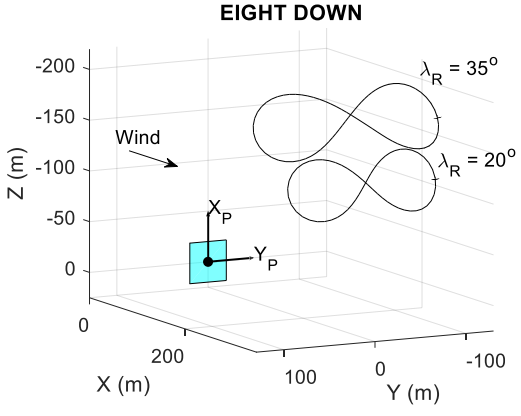

Figure 31. Effect of changing λ_R.

An F8 pattern can be seen as two small circles on each side joined at the centre of the lemniscate. Each side-circle's radius is smaller than typical values for circular reel out. As a result, the angle of attack and sideslip variation can be large, although the former can be alleviated using Eq. (15). Figure 32 demonstrate the controller's effectiveness in keeping α close to its 6° set point through a typical F8 reel-out cycle. This result confirms that the α-suppression controller can be used on both circular and figure-of-eight flight.

https://doi.org/10.5194/wes-2026-69
Preprint. Discussion started: 23 April 2026

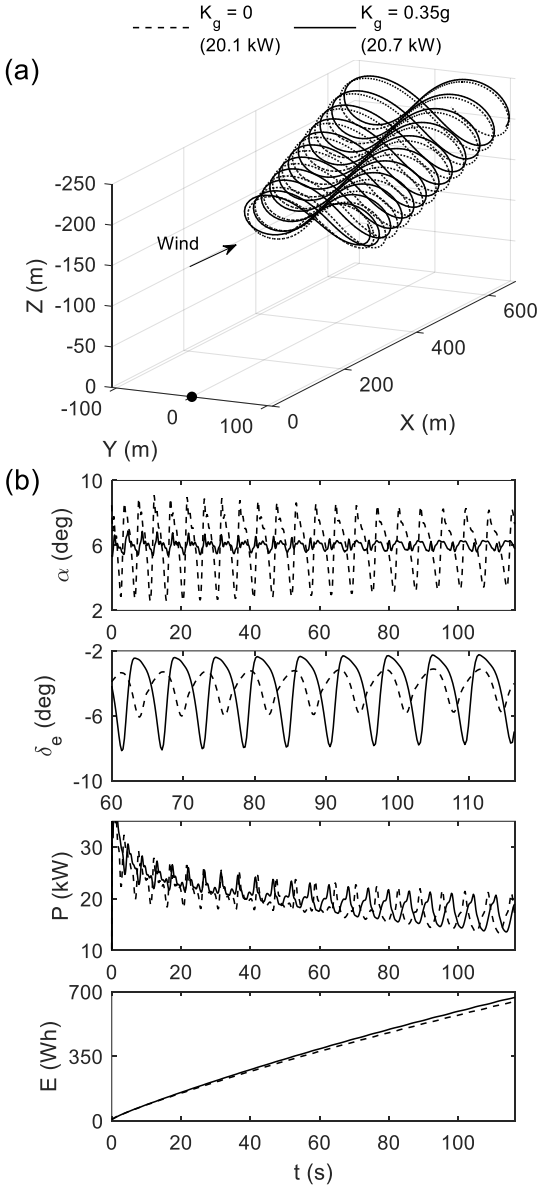

555 **Figure 32. Eight-down reel out without and with α-suppression control.**

9 Conclusions

This paper has shown that by relaxing the path-following requirement, a simple proportional-integral feedback system can provide accurate flight control during circular-pattern reel out. The key enabling idea is in tracking the roll angle on a non-
560 static reference frame. In its simplest form, the controller achieves accurate path following using only ailerons while requiring no air data from a pitot tube. This capability could enable rapid control law development and testing of new AWES

https://doi.org/10.5194/wes-2026-69
Preprint. Discussion started: 23 April 2026

eawe european academy of wind energy
Open Access WIND ENERGY SCIENCE DISCUSSIONS

prototypes. Future improvements can implement more advanced controllers, such as nonlinear dynamic inversion, for the same roll-angle tracking idea but with higher performance. Additionally, recognising that AWES are self-oscillating systems opens up a new class of nonlinear controllers with great potential for the sector. An example of leveraging the inherent limit cycle property to improve performance is provided in the extension to the pitch control loop. By adding a proportional pitch angle feedback term to the elevator, angle-of-attack oscillation can be significantly reduced. Doing so enables the kite to spend more time in its optimal lift-to-drag condition and results in more power. Lastly, an additional PI loop that adjusts circular flight radius provides indirect control of the kite's angular velocity. This property can be exploited to enable phase-synchronisation of multiple kites in a farm configuration. The proportional-integral architecture also positions the controller as a suitable baseline system for benchmarking more advanced control laws. All of the above developments contribute to making AWES safer and more efficient, thereby bringing them one step closer to commercial use.

Appendix A: Earth-to-reference-plane transformation

The Euler roll, pitch, and yaw angles on the reference plane $[\phi_R, \theta_R, \psi_R]$ are obtained from their Earth-axis counterparts $[\phi, \theta, \psi]$ and the reference plane's elevation and azimuth angles $[\lambda_R, \zeta_R]$. This procedure is outlined in Eqs. (A1-A7). Subscripts E, B, and R to denote Earth, body, and reference frames, respectively.

$$\boldsymbol{q}_{EB} = \begin{bmatrix} \cos(\psi/2) \\ 0 \\ 0 \\ \sin(\psi/2) \end{bmatrix} \otimes \begin{bmatrix} \cos(\theta/2) \\ 0 \\ \sin(\theta/2) \\ 0 \end{bmatrix} \otimes \begin{bmatrix} \cos(\phi/2) \\ \sin(\phi/2) \\ 0 \\ 0 \end{bmatrix} \tag{A1}$$

$$\boldsymbol{q}_{ER} = \begin{bmatrix} \cos(\zeta_R/2) \\ 0 \\ 0 \\ \sin(\zeta_R/2) \end{bmatrix} \otimes \begin{bmatrix} \cos\left((\lambda_R + \pi/2)/2\right) \\ 0 \\ \sin\left((\lambda_R + \pi/2)/2\right) \\ 0 \end{bmatrix} \otimes \begin{bmatrix} \cos(\pi/2) \\ \sin(\pi/2) \\ 0 \\ 0 \end{bmatrix} \tag{A2}$$

$$\boldsymbol{q}_{BR} = \boldsymbol{q}_{EB}^{-1} \otimes \boldsymbol{q}_{ER} = \begin{bmatrix} \eta \\ \epsilon_1 \\ \epsilon_2 \\ \epsilon_3 \end{bmatrix} \tag{A3}$$

where η, ϵ_1, ϵ_2, and ϵ_3 are the four elements in the 4 x 1 matrix $\boldsymbol{q}_{BR}$. This gives a direction cosine matrix $\boldsymbol{R}_R^B$ of dimension 3 x 3

$$\boldsymbol{R}_R^B = \boldsymbol{I} + 2\eta S(\boldsymbol{\epsilon}) + 2S(\boldsymbol{\epsilon})S(\boldsymbol{\epsilon}) \tag{A4}$$

https://doi.org/10.5194/wes-2026-69
Preprint. Discussion started: 23 April 2026

eawe european academy of wind energy
Open Access WIND ENERGY SCIENCE DISCUSSIONS

where $S(\boldsymbol{\epsilon})$ is the skew-symmetric matrix

585

$$S(\boldsymbol{\epsilon}) = \begin{bmatrix} 0 & -\epsilon_3 & \epsilon_2 \\ \epsilon_3 & 0 & -\epsilon_1 \\ -\epsilon_2 & \epsilon_1 & 0 \end{bmatrix} \tag{A5}$$

Substituting Eq. (A5) into Eq. (A4) and expand

$$\boldsymbol{R}_R^B = \begin{bmatrix} R_{R,11}^B & R_{R,12}^B & R_{R,13}^B \\ R_{R,21}^B & R_{R,22}^B & R_{R,23}^B \\ R_{R,31}^B & R_{R,32}^B & R_{R,33}^B \end{bmatrix} = \begin{bmatrix} 1-2(\epsilon_2^2+\epsilon_3^2) & 2(\epsilon_1\epsilon_2-\eta\epsilon_3) & 2(\epsilon_1\epsilon_3+\eta\epsilon_2) \\ 2(\epsilon_1\epsilon_2+\eta\epsilon_3) & 1-2(\epsilon_1^2+\epsilon_3^2) & 2(\epsilon_2\epsilon_3-\eta\epsilon_1) \\ 2(\epsilon_1\epsilon_3-\eta\epsilon_2) & 2(\epsilon_2\epsilon_3+\eta\epsilon_1) & 1-2(\epsilon_1^2+\epsilon_2^2) \end{bmatrix} \tag{A6}$$

590 which is based on Eq. (6.215) in (Egeland and Gravdahl, 2003) but with η^2 replaced by $1-\epsilon_1^2-\epsilon_2^2-\epsilon_3^2$. From here, the reference-plane Euler angles can be obtained

$$\begin{bmatrix} \phi_R \\ \theta_R \\ \psi_r \end{bmatrix} = \begin{bmatrix} \text{atan2}\left(R_{R,23}^B, R_{R,33}^B\right) \\ -\arcsin\left(R_{R,13}^B\right) \\ \text{atan2}\left(R_{R,12}^B, R_{R,11}^B\right) \end{bmatrix} = \begin{bmatrix} \text{atan2}(2(\epsilon_2\epsilon_3-\eta\epsilon_1), 1-2(\epsilon_1^2+\epsilon_2^2)) \\ -\arcsin(2(\epsilon_1\epsilon_3+\eta\epsilon_2)) \\ \text{atan2}(2(\epsilon_1\epsilon_2-\eta\epsilon_3), 1-2(\epsilon_2^2+\epsilon_3^2)) \end{bmatrix} \tag{A7}$$

Appendix B: Earth-to-production-plane transformation

The production plane P is defined by its origin, which has an Earth-axis coordinates $[P_X, P_Y, P_Z]$, elevation angle λ_P, and
595 azimuth angle ζ_P. If the kite's position on the Earth axis is $[X, Y, Z]$, its coordinates $[X_P, Y_P, Z_P]$ on the production plane is found using Eqs. (A8-A10)

$$\boldsymbol{q}_{EP} = \begin{bmatrix} \cos(\zeta_P/2) \\ 0 \\ 0 \\ \sin(\zeta_P/2) \end{bmatrix} \otimes \begin{bmatrix} \cos((\lambda_P+(\pi/2))/2) \\ 0 \\ \sin((\lambda_P+(\pi/2))/2) \\ 0 \end{bmatrix} \otimes \begin{bmatrix} \cos(\pi/2) \\ \sin(\pi/2) \\ 0 \\ 0 \end{bmatrix} \tag{A8}$$

$$\boldsymbol{R}_E^P = \boldsymbol{R}(\boldsymbol{q}_{EP}^{-1}) \tag{A9}$$

$$\begin{bmatrix} X_P \\ Y_P \\ Z_P \end{bmatrix} = \boldsymbol{R}_E^P \left(\begin{bmatrix} X \\ Y \\ Z \end{bmatrix} - \begin{bmatrix} P_X \\ P_Y \\ P_Z \end{bmatrix} \right) \tag{A10}$$

https://doi.org/10.5194/wes-2026-69
Preprint. Discussion started: 23 April 2026

eawe european academy of wind energy
Open Access WIND ENERGY SCIENCE DISCUSSIONS

Appendix C: stability proof of the angle-of-attack-oscillation suppression controller

The differential equation for angle of attack (Eq. (12)) is reproduced below

$$\dot{\alpha} = -\frac{1}{2}\frac{\rho V S}{m} C_L - (p\cos\alpha + r\sin\alpha)\tan\beta + \frac{g}{V}\left(\frac{\cos\phi\cos\theta\cos\alpha + \sin\theta\sin\alpha}{\cos\beta}\right) + q \tag{A11}$$

where C_L is the lift coefficient. Presume that aerodynamic lift is within the linear region, the lift coefficient can then be decomposed into the zero-lift, angle-of-attack, and elevator components

$$C_L = C_{L_0} + C_{L_\alpha}\alpha + C_{L_{\delta_e}}\delta_e \tag{A12}$$

Substitute Eq. (A12) into (A11) assume that the sideslip β angle is close to zero, giving $\tan\beta = 0$ and $\cos\beta = 1$. We have

$$\dot{\alpha} = -\frac{1}{2}\frac{\rho V S}{m}\left(C_{L_0} + C_{L_\alpha}\alpha + C_{L_{\delta_e}}\delta_e\right) + \frac{g}{V}(\cos\phi\cos\theta\cos\alpha + \sin\theta\sin\alpha) + q \tag{A13}$$

Denote the error signal in the angle-of-attack feedback loop as $e = \alpha - \alpha_{SP}$ and the integrated error as $e_i = \int e\,dt$. If α_{SP} is static (i.e., a constant), $\dot{e} = \dot{\alpha}$. A Lyapunov function can be defined as

$$H = \frac{1}{2}k_i e_i^2 + \frac{1}{2}e^2 \tag{A14}$$

where k_i is a constant. Differentiating Eq. (A14) gives

$$\dot{H} = k_i e_i \dot{e}_i + e\dot{e} = k_i e_i e + e\dot{\alpha} \tag{A15}$$

Substituting Eq. (A13) into (A15)

$$\dot{H} = k_i e_i e + e\left[-\frac{1}{2}\frac{\rho V S}{m}\left(C_{L_0} + C_{L_\alpha}\alpha + C_{L_{\delta_e}}\delta_e\right) + \frac{g}{V}(\cos\phi\cos\theta\cos\alpha + \sin\theta\sin\alpha) + q\right] \tag{A16}$$

Equation (A16) can be rearranged into

$$\dot{H} = e\left(k_i e_i - \frac{1}{2}\frac{\rho V S}{m}C_{L_{\delta_e}}\delta_e + \frac{g}{V}\sin\theta\sin\alpha\right) - e\frac{1}{2}\frac{\rho V S}{m}\left(C_{L_0} + C_{L_\alpha}\alpha\right) + e\frac{g}{V}\cos\phi\cos\theta\cos\alpha + eq \tag{A17}$$

https://doi.org/10.5194/wes-2026-69
Preprint. Discussion started: 23 April 2026

The first term in Eq. (A17) can be rewritten into $-k_e e^2$, where k_e is a constant, by defining the following feedback control law for the elevator

$$\delta_e = \frac{2m}{\rho V S C_{L_{\delta_e}}}\left(k_e e + k_i e_i + \frac{g}{V}\sin\theta \sin\alpha\right) \tag{A18}$$

the remaining terms of Eq. (A17) can be grouped into $eD(t)$ where $D(t)$ is the disturbance function

$$D(t) = -\frac{1}{2}\frac{\rho V S}{m}\left(C_{L_0} + C_{L_\alpha}\alpha\right) + \frac{g}{V}\cos\phi\cos\theta\cos\alpha + q \tag{A19}$$

this gives the Lyapunov derivative

$$\dot{H} = -k_e e^2 + eD(t) \tag{A20}$$

Each term in the disturbance function (A19) is physically bounded for all time, such that the disturbance becomes upper bounded as $|D(t)| \leq \overline{D}$ for some constant $\overline{D} \geq 0$. Applying Young's inequality to the cross-term yields

$$\dot{H} \leq -\frac{k_e}{2}e^2 + \frac{1}{2k_e}D(t)^2 \tag{A21}$$

which a standard ISS condition implying that the closed-loop system is input-to-state stable with respect to the disturbance $D(t)$ (see (Khalil, 2002) for more details).

The control law in Eq. (A18) can be simplified further based on the small angle of attack assumption

$$\delta_e = \frac{2m}{\rho V S C_{L_{\delta_e}}}\left(k_e e + k_i e_i + \frac{g}{V}\alpha\sin\theta\right) \tag{A22}$$

which can be rewritten as

$$\delta_e = -K_p e - K_i e_i + k_\theta \sin\theta \tag{A23}$$

with

https://doi.org/10.5194/wes-2026-69
Preprint. Discussion started: 23 April 2026

$$K_p = \frac{2mk_e}{\rho VSC_{L_{\delta_e}}} \tag{A24}$$

$$K_i = \frac{2mk_i}{\rho VSC_{L_{\delta_e}}} \tag{A25}$$

$$K_\theta = \frac{2mg\bar{\alpha}}{\rho V^2 SC_{L_{\delta_e}}} \tag{A26}$$

where $\bar{\alpha}$ is an upper bound on the angle of attack.

Code and data availability

The simulation model is proprietary and is therefore not available for the public.

Author contributions

DN: funding acquisition, analysis, writing (original draft). APK: software, analysis, writing (review and editing). TV: software, resources. ML: funding acquisition, writing (review and editing). EO: software, resources, methodology, validation, writing (review and editing).

Competing interests

The authors declare that they have no conflict of interest.

Disclaimer

Copernicus Publications remains neutral with regard to jurisdictional claims made in the text, published maps, institutional affiliations, or any other geographical representation in this paper. While Copernicus Publications makes every effort to include appropriate place names, the final responsibility lies with the authors. Views expressed in the text are those of the authors and do not necessarily reflect the views of the publisher.

Financial support

Duc H. Nguyen and Mark H. Lowenberg are supported by the UK Engineering and Physical Sciences Research Council (EPSRC), grant number EP/Y014545/1. Agustí Porta Ko is supported by the AWETRAIN project, which receives funding from the European Union's Horizon Europe research and innovation programme under the Marie Skłodowska-Curie grant

https://doi.org/10.5194/wes-2026-69
Preprint. Discussion started: 23 April 2026

agreement No 101168734. Espen Oland is part of the 3D-CIRCULAR project, which has received funding from the European Health and Digital Executive Agency under the Grant Agreement No 101226256. The contents of this publication are the sole responsibility of the authors and do not necessarily reflect the opinion of the European Union.

References

Ahrens, U., Diehl, M., and Schmehl, R.: Airborne Wind Energy, Green Energy and Technology, Springer Berlin, Heidelberg, Germany, 10.1007/978-3-642-39965-7, 2013.

Basile, L., Berni, M. G., and Celani, A.: Harvesting energy from turbulent winds with reinforcement learning, Europhysics Letters, 152, 43001, doi: 10.1209/0295-5075/ae1ce9, 2025.

Cherubini, A., Papini, A., Vertechy, R., and Fontana, M.: Airborne Wind Energy Systems: A review of the technologies, Renewable and Sustainable Energy Reviews, 51, 1461-1476, doi: 10.1016/j.rser.2015.07.053, 2015.

Cobb, M. K., Barton, K., Fathy, H., and Vermillion, C.: Iterative Learning-Based Path Optimization for Repetitive Path Planning, With Application to 3-D Crosswind Flight of Airborne Wind Energy Systems, IEEE Transactions on Control Systems Technology, 28, 1447-1459, doi: 10.1109/TCST.2019.2912345, 2020.

DeLosRíos-Navarrete, F., González-García, J., Castro-Fernández, I., and Sánchez-Arriaga, G.: A small-scale and autonomous testbed for three-line delta kites applied to airborne wind energy, Wind Energ. Sci., 10, 1153-1166, doi: 10.5194/wes-10-1153-2025, 2025.

Dief, T. N., Fechner, U., Schmehl, R., Yoshida, S., and Rushdi, M. A.: Adaptive Flight Path Control of Airborne Wind Energy Systems, Energies, 13, 667, doi: 10.3390/en13030667, 2020.

Diehl, M.: Airborne Wind Energy: Basic Concepts and Physical Foundations, in: Airborne Wind Energy, edited by: Ahrens, U., Diehl, M., and Schmehl, R., Springer Berlin Heidelberg, Berlin, Heidelberg, 3-22, 10.1007/978-3-642-39965-7_1, 2013.

Egeland, O. and Gravdahl, J.: Modeling and Simulation for Automatic Control, 2nd, Marine Cybernetics, Trondheim, Norway2003.

Fagiano, L., Zgraggen, A. U., Morari, M., and Khammash, M.: Automatic Crosswind Flight of Tethered Wings for Airborne Wind Energy: Modeling, Control Design, and Experimental Results, IEEE Transactions on Control Systems Technology, 22, 1433-1447, doi: 10.1109/TCST.2013.2279592, 2014.

Fernandes, M. C. R. M., Vinha, S., Paiva, L. T., and Fontes, F. A. C. C.: L0 and L1 Guidance and Path-Following Control for Airborne Wind Energy Systems, Energies, 15, 1390, doi: 10.3390/en15041390, 2022.

Fritz, F.: Application of an Automated Kite System for Ship Propulsion and Power Generation, in: Airborne Wind Energy, edited by: Ahrens, U., Diehl, M., and Schmehl, R., Springer Berlin Heidelberg, Berlin, Heidelberg, 359-372, 10.1007/978-3-642-39965-7_20, 2013.

Heydarnia, O., Wauters, J., Lefebvre, T., and Crevecoeur, G.: Optimal Path Planning of Airborne Wind Energy Systems with a Flexible Tether, Journal of Guidance, Control, and Dynamics, doi: 10.2514/1.G008967, 2025.

Jordan, D. W. and Smith, P.: Nonlinear Ordinary Differential Equations - An Introduction for Scientists and Engineers, Oxford University Press, New York2007.

Kelly, M.: From standard wind measurements to spectral characterization: turbulence length scale and distribution, Wind Energy Science, 3, 533-543, doi: 10.5194/wes-3-533-2018, 2018.

Khalil, H. K.: Nonlinear Systems, 3rd, Prentice Hall, New Jersey2002.

Khurshid, Y., Paul, P., Elhesasy, M., Ali, B., Kamra, M. M., Okasha, M., and Dief, T. N.: From inception to commercialization: A systematic review of airborne wind energy systems, Sustainable Energy Technologies and Assessments, 83, 104623, doi: 10.1016/j.seta.2025.104623, 2025.

Loyd, M. L.: Crosswind kite power (for large-scale wind power production), Journal of Energy, 4, 106-111, doi: 10.2514/3.48021, 1980.

Mann, J.: The spatial structure of neutral atmospheric surface-layer turbulence, Journal of Fluid Mechanics, 273, 141-168, doi: 10.1017/S0022112094001886, 1994.

https://doi.org/10.5194/wes-2026-69
Preprint. Discussion started: 23 April 2026

Mohammed, T., Oland, E., and Fagiano, L.: Fault Tolerant Flight Control for the Traction Phase of Pumping Airborne Wind Energy Systems, International Journal of Control, Automation and Systems, doi: 10.1007/s12555-023-0588-z, 2024a.

Mohammed, T., Busk, J., Oland, E., and Fagiano, L.: Large-Scale Reverse Pumping for Rigid-Wing Airborne Wind Energy Systems, Journal of Guidance, Control, and Dynamics, 47, 1748-1758, doi: 10.2514/1.G007859, 2024b.

NASA: Experience with the X-15 Adaptive Flight Control System, National Aeronautics and Space Administraion, 1971.

Nguyen, D. H., Lowenberg, M. H., and Oland, E.: Trimming a rigid-wing airborne wind system for coordinated circular flights, Wind Energy Science, 11, 285-298, doi: 10.5194/wes-11-285-2026, 2026a.

Nguyen, Duc H., Lowenberg, Mark H., and Oland, E.: Improving Power Generation in Rigid-Wing Groundgen Airborne Wind Energy Systems Using Feedback Control—A Parametric Study, Wind Energy, 29, e70109, doi: 10.1002/we.70109, 2026b.

Orzan, N., Leone, C., Mazzolini, A., Oyero, J., and Celani, A.: Optimizing airborne wind energy with reinforcement learning, The European Physical Journal E, 46, 2, doi: 10.1140/epje/s10189-022-00259-2, 2023.

Pereira, A. F. C. and Sousa, J. M. M.: A Review on Crosswind Airborne Wind Energy Systems: Key Factors for a Design Choice, Energies, 16, 351, doi: 10.3390/en16010351, 2023.

Rapp, S., Schmehl, R., Oland, E., and Haas, T.: Cascaded Pumping Cycle Control for Rigid Wing Airborne Wind Energy Systems, Journal of Guidance, Control, and Dynamics, 42, 2456-2473, doi: 10.2514/1.G004246, 2019.

Schmehl, R.: Airborne Wind Energy - Advances in Technology Development and Research, Green Energy and Technology, Springer Singapore, Singapore, 10.1007/978-981-10-1947-0, 2018.

Schmidt, H., de Vries, G., Renes, R. J., and Schmehl, R.: The Social Acceptance of Airborne Wind Energy: A Literature Review, Energies, 15, 1384, 2022.

Trevisi, F.: Conceptual design of windplanes, Department of Aerospace Science and Technology, Polytechnic University of Milan, Milano, Italy, 2024.

Trevisi, F., Croce, A., and Riboldi, C. E. D.: Flight Stability of Rigid Wing Airborne Wind Energy Systems, Energies, 14, 7704, doi: 10.3390/en14227704, 2021.

Vermillion, C., Cobb, M., Fagiano, L., Leuthold, R., Diehl, M., Smith, R. S., Wood, T. A., Rapp, S., Schmehl, R., Olinger, D., and Demetriou, M.: Electricity in the air: Insights from two decades of advanced control research and experimental flight testing of airborne wind energy systems, Annual Reviews in Control, 52, 330-357, doi: 10.1016/j.arcontrol.2021.03.002, 2021.

Vinha, S., Fernandes, G. M., Fernandes, M. C. R. M., and Fontes, F. A. C. C.: Motion Primitives on a Spherical Surface with Application to Tethered Aircraft Guidance, 2025 IEEE 19th International Conference on Control & Automation (ICCA), Tallinn, Estonia, 30 June-3 July, 186-191, doi: 10.1109/ICCA65672.2025.11129856, 2025.